AN ABSTRACT OF THE THESIS OF

Chase H. Simpson for the degree of Master of Science in Civil Engineering presented on November 14, 2018.

Title: A Multivariate Comparison of Drone-Based Structure from Motion and Drone-Based Lidar for Dense Topographic Mapping Applications

Abstract approved: _____
Christopher E. Parrish

Unmanned aircraft systems (UAS), also known as drones, are an increasingly popular method of collecting surveying and mapping data. Two common drone-based mapping techniques are lidar and structure from motion (SfM) photogrammetry, and a frequently-heard (yet nearly impossible to answer) question is: "which is better?" The most common metric for comparison is spatial accuracy, but the two techniques also vary in other key aspects, such as cost, complexity, learning curve, payload requirements, acquisition and processing speeds, and abilities to map under canopy or in vegetation. While there is no "one-size-fits-all" technology or technique, comparisons of drone-based lidar and SfM photogrammetry along all of these different dimensions and various settings can help surveyors and mappers make informed decisions in purchasing and operating UAS-based systems. This study performs these comparisons using data acquired with two remote aircraft at a project site with a robust control network and high-accuracy reference data located in Stevenson, Washington. The results shed light on the relative strengths and weaknesses of UAS-SfM with post processed kinematic (PPK) image georeferencing (UAS-SfM-PPK) and UAS-lidar. The products created using these two techniques typically provide comparable data accuracies with some differences, as a function of terrain, ground cover type and surface texture. Although UAS-SfM-PPK is generally less expensive, imposes less stringent requirements for the remote aircraft, requires less expert knowledge and training, and yields higher data densities, an overarching recommendation from this research is that UAS-SfM-PPK be considered the default,

general-purpose technique for many mapping projects. However, there are a number of specific scenarios in which UAS-lidar is preferable to UAS-SfM-PPK, and it is critical to understand these cases. Additionally, while the combination of UAS-SfM-PPK and UAS-lidar would typically be unnecessarily expensive and complex for most projects, the synergistic use of both techniques could provide an optimal solution for the most demanding projects.

Author keywords: UAS lidar; UAS SfM; structure from motion; aerial lidar; vertical accuracy assessment; topographic mapping; drones; PPK

A Multivariate Comparison of Drone-Based Structure from Motion and Drone-Based Lidar for Dense Topographic Mapping Applications

by
Chase H. Simpson

A THESIS

submitted to

Oregon State University

in partial fulfillment of
the requirements for the
degree of

Master of Science

Presented November 14, 2018
Commencement June 2019

Master of Science thesis of Chase H. Simpson presented on November 14, 2018

APPROVED:

Major Professor, representing Civil Engineering

Head of the School of Civil and Construction Engineering

Dean of the Graduate School

I understand that my thesis will become part of the permanent collection of Oregon State University libraries. My signature below authorizes release of my thesis to any reader upon request.

Chase H. Simpson, Author

ACKNOWLEDGEMENTS

The author would like to acknowledge and express sincere appreciation to the following people for their support and assistance with completing this study:

- Dr. Christopher Parrish for providing funding for this research and assisting with the analysis of the data
- Richie Slocum for helping with the data acquisition and providing his MATLAB expertise to assist with data processing
- Kory Kellum, previously with Klein & Associates, for collecting and completing the initial processing steps for the UAS-lidar data
- Port of Skamania for allowing access to the project site
- Fellow geomatics graduate students and faculty for helping me along this journey
- Leica Geosystems and David Evans & Associates for providing the surveying equipment and processing software
- PacTrans for funding portions of this study

TABLE OF CONTENTS

LIST OF FIGURES

LIST OF FIGURES (Continued)

Figure Page

LIST OF TABLES

1 Introduction

Unmanned Aircraft Systems (UASs) have rapidly progressed and generated increasing interest for a wide range of applications due, in large part, to the miniaturization and affordability of many technologies, such as inertial navigation, GNSS positioning, batteries, remote sensing payloads, and computer processing. The reduced cost and size of UAS resulting from these technological advancements in combination with efforts of aviation authorities to open the airspace to commercial use of small UAS, has increased the viability for UAS commercial applications in the mapping industry. The Federal Aviation Administration (FAA) in the USA has specifically made this possible through the release of the Small Unmanned Aircraft System Rule, officially Part 107 of Title 14 Code of Federal Regulations (14 CFR) (Federal Aviation Administration, 2016).

One of the many benefits for the application of UAS is their ability to collect high-resolution remotely sensed data, typically acquired at a significantly lower altitude when compared to manned aircrafts (Fonstad *et al.*, 2012; Harwin and Lucieer, 2012; Mancini *et al.*, 2013; Micheletti, Chandler and Lane, 2015; Marteau *et al.*, 2017). However, a side effect to their lower altitude and insufficient flight endurance is that they are unable to efficiently capture data for larger areas, typically greater than 2 square kilometers, of interest where manned aircraft excel. This limitation for UASs is partially outweighed by having the ability to quickly interchange multiple sensors, often referred to as payloads, at the project site and being able to complete repeat mapping missions to track changes throughout the area of interest (AOI) at a significantly lower cost than manned aircraft.

The ability to equip UAS with a wide variety of payloads allows for the collection of a diverse range of remotely-sensed data. Recently, two of the most popular payloads for the application of topographic mapping from UAS are: 1) RGB cameras in combination with structure from motion and multi view stereo (SfM-MVS) processing techniques, and 2) lidar. The primary difference between these two payloads is that RGB imagery is captured using a passive sensor, while lidar is an active sensor. An active sensor uses its own source of electromagnetic energy and measures the returning energy that has been reflected back to the sensor. Thus, active sensors, such as lidar, are relatively invariant to

ambient lighting conditions. However, there are inherent tradeoffs involved, in that active sensor systems are typically more expensive, due to the increased hardware requirements (transmitter, and receiver) and are susceptible to angular and linear errors due to the number of moving parts used to derive the positions of each point (Pilarska *et al.*, 2016). In contrast, a passive sensor, such as an RGB camera, is reliant on capturing energy reflected off of an object originating from an external source, typically the sun. This dependence on an external source allows for the sensors to be much simpler, but the quality of data captured can be largely affected by environmental factors. For example, when the sun is the external energy source, occlusions in the acquired data can be created by shadows throughout the scene, typically caused by clouds or terrestrial objects (e.g. trees, and structures). This sensitivity to environmental factors is similar to the same limitations faced by traditional photogrammetry.

The field of photogrammetry is well over 150 years old, and, interestingly, predates the invention of both the airplane and the camera (Albertz, 2007). Conventional photogrammetry relies on precisely calibrated, stable cameras (so-called metric-mapping cameras) operated from precisely flown platforms (i.e., stable imaging geometry). This type of operation worked well before the advent of high-powered digital computers, as the geometry, and, hence, the mathematics of analytical photogrammetry can be highly-constrained with such rigid control over the acquisition and camera parameters. Meanwhile, SfM and MVS were developed much more recently—starting in the 1980s—and, interestingly, somewhat independently of conventional photogrammetry, being led by the computer vision community specifically through the development of the SIFT algorithms implemented for image matching (Lowe, 1999; Fonstad *et al.*, 2012). By leveraging advanced image matching algorithms from computer vision, as well as much greater image overlap, SfM + MVS enable precise 3D reconstruction and coordinate determination from imagery from uncalibrated, consumer-grade, cameras (Fonstad *et al.*, 2012; Westoby *et al.*, 2012; Micheletti, Chandler and Lane, 2015). Furthermore, the SfM-MVS algorithms and workflows have been automated to the point that users of commercial software can generate point clouds and orthomosaics with little human time (although processing time can be lengthy). A discussion of the overall workflow

implemented by these software is beyond the scope of this thesis but the reader is referred to (Fonstad *et al.*, 2012; Westoby *et al.*, 2012; Micheletti, Chandler and Lane, 2015).

SfM and photogrammetry are sometimes characterized as different fields, causing users to be reluctant to implement SfM-MVS for applications previously fulfilled by traditional photogrammetry. However, SfM is, in fact, a form of photogrammetry, as it meets the basic definition of photogrammetry, as given by ASPRS:

> Photogrammetry is the art, science and technology of attaining reliable information about physical objects and the environment through the process of recording, measuring, and interpreting photographic images and patterns of electromagnetic radiant energy and other phenomena (Alspaugh, 2004).

Furthermore, despite the fact that SfM incorporates new algorithms from the field of computer vision, SfM and conventional photogrammetry are actually more similar than they are different.

While both SfM-MVS and lidar are relatively new technologies for topographic mapping, lidar has a longer history of use within the surveying and mapping community, starting in approximately the mid-to-late 1990s. Traditionally, lidar has been operated from terrestrial platforms, such as tripods (called terrestrial lidar or 3D laser scanning), mobile platforms, such as trucks or SUVs (mobile lidar), or conventional aircraft (airborne lidar). Recent progress in the miniaturization of lidar sensors and positioning systems has enabled lidar to also be installed on UAS (UAS-lidar). In the most common implementations, lidar relies on time-of-flight measurements of laser pulses, which, in the case of mobile and airborne lidar, are combined with GNSS-aided INS post-processed trajectories, scan angles, and calibration data in a laser geolocation equation to produce georeferenced point clouds. Due to the number of existing papers, reports, and books on lidar technology, this thesis does not include a detailed overview of the technology; interested readers are referred to ASPRS *Manual of Airborne Topographic Lidar* (Renslow, 2012) and *Topographic Lidar Ranging and Scanning Principles and Processing* (Shan and Toth, 2008).

With these recent technological developments, surveyors and mapping professionals need more information about how these smaller sensors and new processing methods (SfM photogrammetry and UAS-compatible laser scanners) compare. Unfortunately, such comparisons have been complicated by the following: 1) recent emergence of both techniques, 2) abundant, but sometimes conflicting and unclear information available online; 3) differences along a number of dimensions, such as accuracy, cost, and ease-of-use. To help alleviate these complications, this study assesses UAS-SfM with post processed kinematic (PPK) image georeferencing, to be referred to as UAS-SfM for the remainder of this paper, and UAS-lidar using a dense reference control dataset and compares the results to terrestrial lidar, a well-tested and highly regarded remote sensing platform typically used to collect dense 3D data sets, in order to aid with purchasing decisions and the selection of the most applicable technology for a particular project.

The specific goals of this study are to: (i) provide information on how two common drone-based mapping techniques, UAS-SfM and UAS-lidar, perform relative to one another through a quantitative comparison with terrestrial lidar and highly accurate control check points established using traditional survey techniques; (ii) provide a qualitative assessment that discusses the key benefits and limitations of each technique such as cost, system complexity, learning curve, remote aircraft payload requirements; and (iii) summarize the advantages and disadvantages of each to aid professionals in selecting the most advantageous technique based on project requirements.

2 Materials & Methods

2.1 Study Site

The area of interest (AOI) is located near the Port of Skamania at the waterfront in Stevenson, Washington (Figure 1). It was selected for the evaluation of the various sensor types, due to its diverse site characteristics, Class G (uncontrolled) airspace, and ease of access for all data collection parties, Oregon State University from Corvallis, Oregon, and Klein and Associates from Hood River, Oregon.

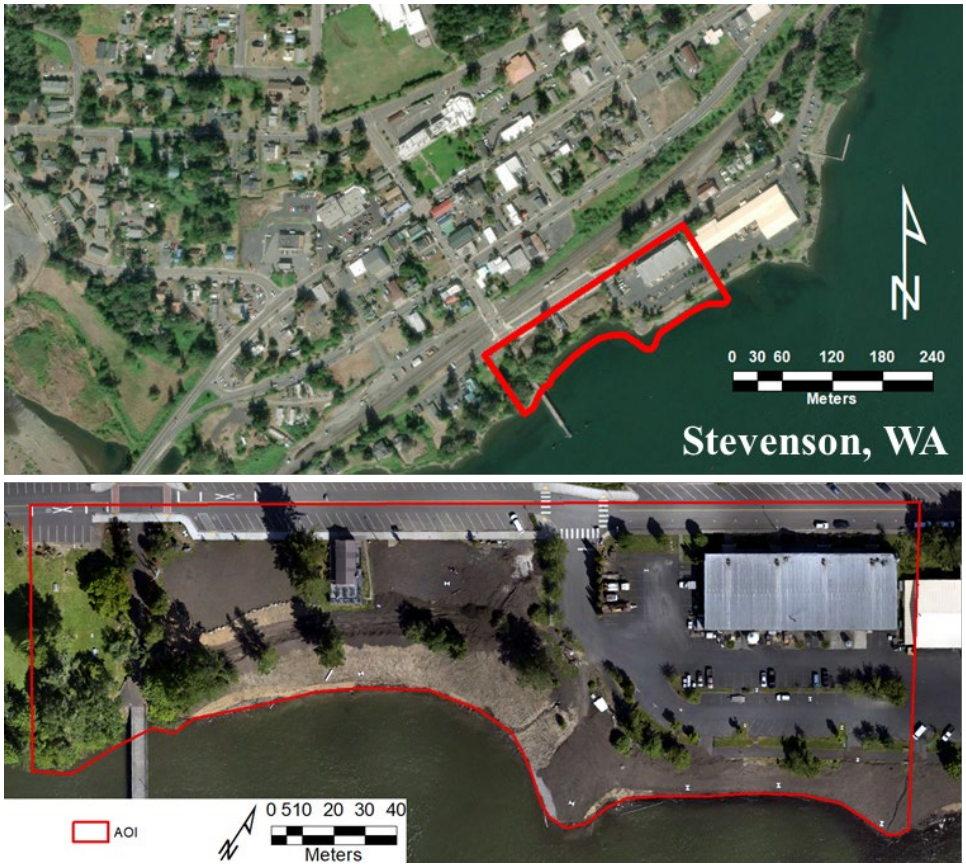

Figure 1: A map depicting the location of the area of interest for this study.

The multiple surface types found throughout the AOI include grass, concrete, asphalt, multiple soil types, and small sections of river rock (gravel), as shown in Figure 2. In addition to the various surface types the AOI also contains a diverse set of topographic features such as: large gradients cause by soil stock piles and manmade slopes, buildings, curb, sidewalk, roadways, vehicles, street lights, and various species of vegetation.

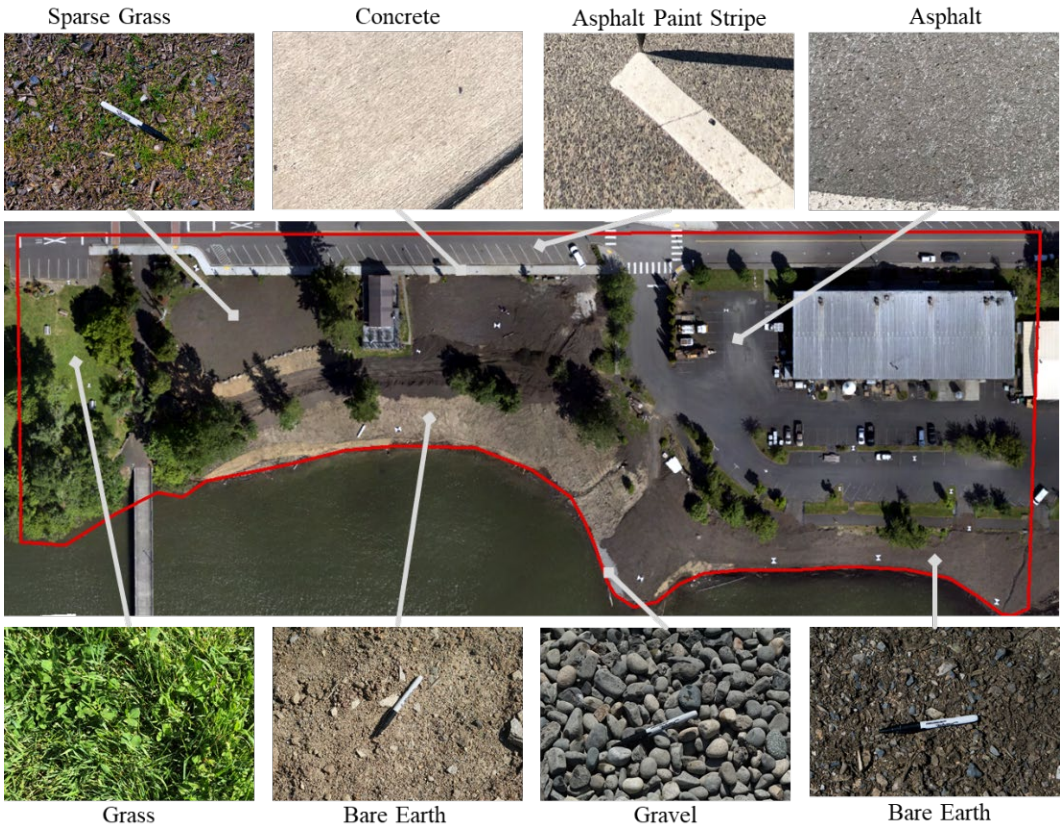

Figure 2: Examples of the various surface types found throughout the area of interest.

2.2 Control Network

2.2.1 Control Network Data Collection

A control network was established across the site to georeference the terrestrial lidar and to provide adequate ground control points (GCPs) and check points (CPs) for the horizontal and vertical accuracy assessment of the aerial lidar and SfM data. This control network consists of evenly-distributed aerial targets, terrestrial box targets, and photo-identifiable features (e.g. sidewalk joints, paint stripes, etc.). Examples of the various control and check points can be seen in Figure 3 (a-d). The aerial targets are iron cross targets, approximately 1 m^2 in size, nailed or weighted to the ground to ensure they did not move throughout the various surveys (control network, terrestrial lidar, and aerial mapping). In addition to the targets mentioned above, vertical checkpoints were also collected on various surface types (e.g. pavement, bare earth, and grass) under various

conditions (e.g. non-obstructed visibility, and under dense tree canopy). The total quantity of these targets is summarized in Table 1.

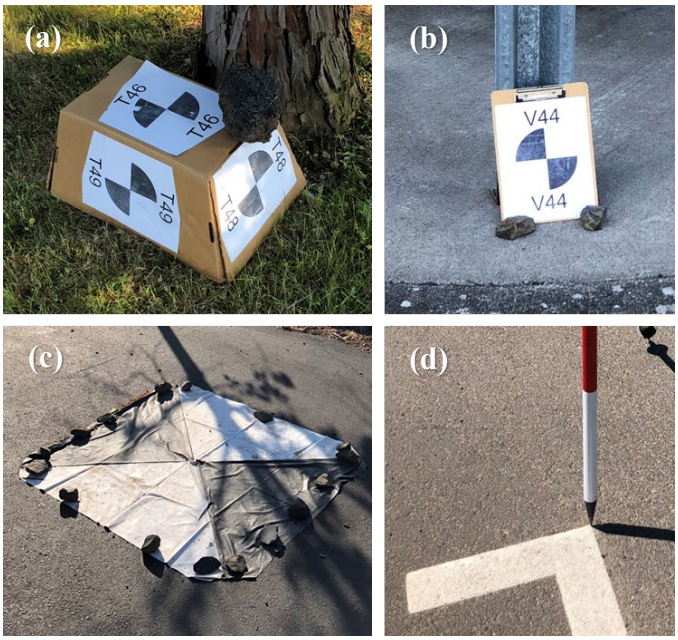

Figure 3 (a-d): Examples of the multiple control/checkpoint targets used in the control survey.

Table 1: Summary of the quantity and type of control/check points acquired in the control survey.

Surface Type	QTY
GNSS Control	5
Terrestrial Lidar Target	27
Iron Cross Targets	14
Vertical Check Points	110
Grass	*26*
Bare Earth	*32*
Concrete	*9*
Asphalt	*43*
Identifiable Features	16
ADA mat corner	*5*
Paint stripe	*11*
Vertical Check Points Under Canopy	21
Grass	*7*
Bare Earth	*3*
Concrete	*1*
Asphalt	*10*

The coordinates for the GCPs and CPs were derived by combining data from two surveying technologies: a multi-frequency, Leica GS14, GNSS receiver capable of utilizing the Oregon Real-Time Network (ORGN) as well as logging static GNSS RINEX files, Figure 4 (a); and a Leica TS15P 3" total station with a Leica 360° prism, Figure 4 (b-c). A total of 5 static GNSS control points were established and observed for durations around 60 to 180 minutes. The Leica TS15P total station was set up in three different positions from which all aerial targets and GNSS control points were observed multiple times in the direct and reverse faces of the instrument. The data acquisition technologies and methodology resulted in a robust dataset that was optimally adjusted through the use of a least squares adjustment using *MicroSurvey STAR*NET Pro* resulting in a more accurate ground truth model that will be utilized for terrestrial lidar registration and comparison purposes.

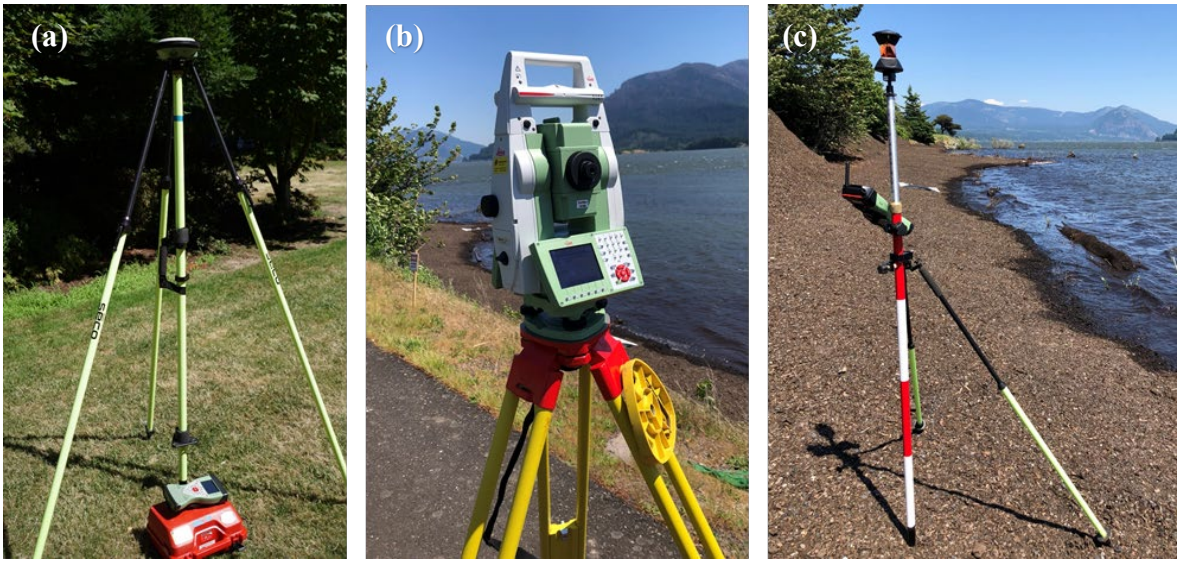

Figure 4 (a-c): The various survey instruments used to complete the control survey of the AOI. (a) is a Leica GS14 Receiver mounted on top of a seco 2 meter fixed height tripod; (b) is a Leica TS14P 3" Robotic Total station; (c) shows the prism rod with 360 degree prism and Leica CS15 Data collector used to remotely control the total station.

2.2.2 Control Network Processing/Adjustment

The control survey was adjusted using *MicroSurvey STAR*NET Pro*. The static GNSS observation data for the 5 GNSS control points, spaced evenly throughout the area of

interest, were first uploaded and processed in the National Geodetic Survey's Online Positioning User Service (OPUS) (National Geodetic Survey, 2018). Stations that were observed for 15 minutes to 2 hours were upload to OPUS Rapid Static, while stations that were observed continuously for greater than 2 hours were upload to OPUS Static. Table 2 summarizes the GNSS observation times for each OPUS solution that was input into *STAR*NET Pro*.

Table 2: Summary of Static and Rapid Static GNSS observations submitted to NGS's OPUS for corresponding stations.

Static Observations	Duration	Rapid Static Observations	Duration
PSK03	1h 58m	P44	1h 07m
PSK03	2h 49m	PSK01	1h 04m
PSK02	5h 22m	PSK02	0h 52m
		PSK04	1h 08m

The next step required importing the raw total station observations for all 3 total station positions into *STAR*NET Pro*. These observations included the target ID, horizontal angle, distance, vertical angle, and rod height. Prior to adjusting any data a few project settings needed to be established. For this data, the coordinate system is set as Washington State Plane South Zone (4602) NAD83(2011) epoch:2010.000 and the vertical datum is NAVD88 (Geoid12B) with units of meters.

The general workflow for adjusting this data includes adjusting each of the total station vectors from each setup for each point observed to the GNSS control coordinates. In order to weight the total station observations the following stochastic model about the measurement equipment was implemented, see table 3 below. These stochastic model values were derived from averaging repeat observation, instrument specification sheets, and minor iterative adjustments during outlier removal.

Table 3: The corresponding values used for each parameter of the stochastic model and comments on how that value was determined.

Parameters	Value	Comments
Conventional		
Distance Constant (m)	0.001	Instrument spec
Distance PPM	1.50	Instrument spec
Angle (sec)	6.55	Multiplied direction value by $\sqrt{2}$
Directions (sec)	4.63	Average direction error of 8 repeat observations for each of the following points (GPS01-GPS04, and P44) from 3 total station positions
Azimuth/Bearing (sec)	1.00	Default (not applicable)
Zenith (sec)	6.18	Average direction error of 8 repeat observations for each of the following points (GPS01-GPS04, and P44) from 3 total station positions
Elev Diff Constant	0.001	Default (not applicable)
Elev Diff PPM	0.00	Default (not applicable)
Centering Errors		
Horiz Inst. (m)	0.0015	Although not set up over point - this error can account for movement in total station throughout the setup
Horiz Target (m)	0.0035	Assuming a 6' bubble on a 2 meter rod
Vertical (m)	0.000003	Assuming a 6' bubble on a 2 meter rod

To identify/remove the outliers in the datasets within *STAR*NET Pro* the following procedure was implemented after processing using the initial stochastic model outlined above:

1. Temporarily removed any observation that had a standard residual greater than 6.0
2. Re-adjusted stochastic model with initial outliers removed with the goal of achieving a total error factor as close to unity as possible. If the value was greater than 1 the stochastic model overestimated the error parameters; similarly if the value was less than 1 the model was underestimating the error parameters.
3. After creating a new stochastic model each rejected observation was added individually.
    a. If the standard residual was less than 3.0, and the total error factor was not greatly affected by its addition, the added observation was kept; if not, the observations was removed.

   b. After going through all of the rejected observations, the stochastic model was re-adjusted as needed.
4. After the stochastic model was re-adjusted, the remaining outliers were added individually.
5. If any outliers were accepted under the new stochastic model then the stochastic model was adjusted once more.
6. Steps 3-5 were iterated until there were no rejected observations accepted in the most recent stochastic model.

After completing the observation outlier rejection procedure described above, there were no rejected observations. The resulting stochastic model parameters were determined and are shown in Table 4 below. Note that the final parameters correspond well with the initial values previously indicated.

Table 4: Summary of the final stochastic model used when processing the control network within Star*NET.

Parameters	**Value**
Conventional	
Distance Constant (m)	0.0015
Distance PPM	1.5000
Angle (sec)	1.5000
Directions (sec)	2.5000
Azimuth/Bearing (sec)	1.0000
Zenith (sec)	8.0000
Elev Diff Constant	0.0010
Elev Diff PPM	0.0000
Centering Errors	
Horiz Inst. (m)	0.0015
Horiz Target (m)	0.0020
Vertical (m)	0.0020

In order to quantify the accuracy of the final adjusted coordinates for the ground control points and checkpoints, the following summary statistics were calculated based on the propagated error uncertainties reported by *STAR*NET* for each point, shown in the Table 5. The following conversion factors were used to scale the calculated RMSE values to a 95% confidence level. These scalars are applied based on the assumption that the

uncertainties are normally distributed. Additionally, the final dispersion of the control/check points can be viewed in Figure 5.

$$1D\ 95\%\ Confidence = 1.9600 \cdot (1D\ RMSE) \quad (1)$$

$$2D\ 95\%\ Confidence = 1.7308 \cdot (2D\ RMSE) \quad (2)$$

$$3D\ 95\%\ Confidence = 1.6166 \cdot (3D\ RMSE) \quad (3)$$

Table 5: Combined statistical summary of all processed control points (vertical CPs, Horizontal CPs, and 3D GCPs, and GNSS stations).

Summary Statistics	3D (m)	NE (m)	E (m)	N (m)	U (m)
Minimum	0.0132	0.0052	0.0040	0.0031	0.0121
Maximum	0.0159	0.0098	0.0070	0.0080	0.0131
Average	0.0145	0.0072	0.0051	0.0051	0.0125
Std. Deviation	0.0006	0.0011	0.0006	0.0011	0.0002
RMSE	0.0145	0.0073	0.0052	0.0052	0.0125
95% Confidence	0.0234	0.0127	0.0101	0.0102	0.0245

Figure 5: Overview map of the AOI showing the resulting control and check points of the control network survey.

2.3 Terrestrial Lidar

2.3.1 Terrestrial Lidar Data Collection

Terrestrial lidar data of the site was collected in 10 separate scans using a Leica P40 laser scanner to serve as reference data. Each scan duration was approximately 15 minutes, resulting in an average point spacing of 0.01 meters on orthogonal surfaces at a distance of 30 meters from the scanner. Note the point density decreases as the range from the scanner is increased. Additionally, RGB imagery was co-acquired at each scan position to colorize the point cloud. When selecting scanning locations the follow criteria were considered:

- Line of sight to a minimum of 5 registration targets
- Consistent overlap with adjacent scans to aid in cloud to cloud registration when post processing
- Unobstructed line-of-site of surrounding terrain to optimize scanned area per set up (i.e. no nearby obstructions such as trees, cars, structures, etc.)
- Good sky visibility for GNSS solution

To aid in georeferencing the terrestrial lidar data, a Leica GNSS receiver receiving real-time corrections from the Oregon Real-Time GNSS Network (ORGN), as well as logging static GNSS RINEX files, was mounted on top of the scanner for each position as shown in Figure 6. The scanner was left at each scan position for a minimum of 20 minutes, approximately 5 minutes longer than the scanning duration, to ensure the GNSS observation time was adequate to attain an OPUS-RS solution. The OPUS-RS solution obtained from processing the static observations are to be the primary coordinates used for each scan position. As a redundancy, in case OPUS-RS was unable to attain a fixed solution, the ORGN real-time coordinates would be used.

Figure 6: The Leica P40 Lidar scanner with a Leica GS14 GNSS antenna mounted on its top during one of the 10 scan position observations.

2.3.2 Terrestrial Lidar Processing

The terrestrial lidar was registered and classified using Leica Geosystems *Cyclone v9.1.4*. Two registration methods were used in unison to complete the geo-referencing and registration of the 10 scan positions: a manual target-based technique with scanner origin from GPS observations, and a cloud-to-cloud technique. For the target-based technique circular black/white targets printed on 8.5in x 11in sheets of paper and glued to boxes and clipboards were distributed throughout the AOI when establishing the control network. These targets were used as common tie points between the numerous scan positions to aid in scan registration. They also allowed the scanner's origin to be indirectly transformed, or georeferenced, to align with the coordinate system of the targets, as specified in the previous section. Images of a single black/white target set in the AOI and extracted from the point cloud are shown in Figure 7 (a, b).

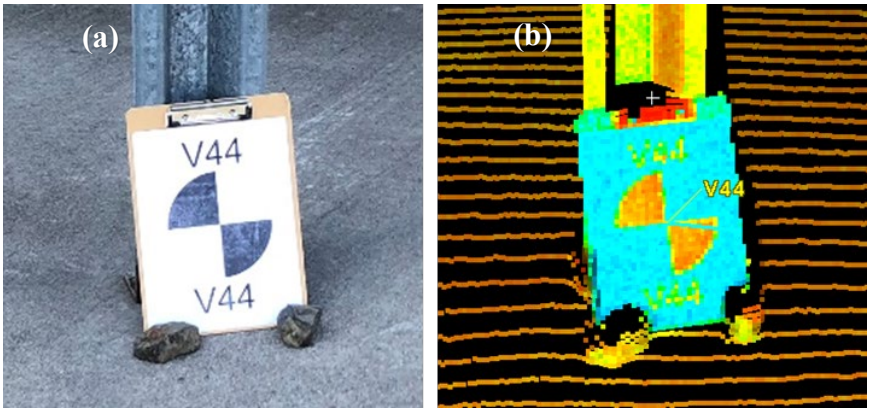

Figure 7 (a, b): One of the numerous black and white targets distributed throughout the AOI to be used in the georeferencing/registration process for the terrestrial lidar scans. Where (a) is the photo taken at the site of target V44, and (b) is the same target as seen in the terrestrial lidar point cloud from scan position 2.

The second method, cloud-to-cloud, uses an automated matching algorithm (Iterative Closest Point), which assigns the closest point in one scan (scan B) as a match to another point in a second scan (scan A). The numerous point pairs are then used to determine the parameters to transform scan B to scan A. One limitation of cloud-to-cloud registration is that it requires the scans be approximately aligned to each other prior to implementing the cloud-to-cloud registration. To accomplish this initial alignment, scan B was visually aligned to scan A through a series of manual translations and rotations.

Three methods were implemented to assess the final registration of the terrestrial lidar scans: evaluation of root mean square (RMS) residuals of the cloud to cloud constraints, evaluation of target residuals, and visual inspection. The purpose of the first method, evaluating the cloud-to-cloud comparison, was to assess the relative error between the various scan positions and to quantify the overall relative accuracy of the registration process. The second method, the evaluation of registration target residuals compared to the control survey coordinates, was used to determine the overall registration accuracy of the final registered product. The results shown in Table 6 indicate that the overall 3D accuracy of the targets was 1.4 cm at a 95% confidence level with a standard deviation of 0.6 cm. It should be noted that this error does not fully represent the global accuracy of the data, due to possible user errors introduced when processing the data (i.e. the exact same location of a target might not have been identified in all of the scans).

Table 6: The statistical summary of the errors for the control targets used in registering/georeferencing the 10 terrestrial scans together.

Summary Statistics	3D (m)	EN (m)	E (m)	N (m)	U (m)
Minimum	0.0011	0.0003	-0.0249	-0.0118	-0.0067
Maximum	0.0269	0.0257	0.0093	0.0040	0.0229
Average	0.0065	0.0046	-0.0018	-0.0002	0.0019
Std. Deviation	0.0061	0.0046	0.0055	0.0030	0.0058
RMSE	0.0089	0.0065	0.0058	0.0030	0.0061
95% Confidence	0.0143	0.0112	0.0113	0.0058	0.0119

The final verification method, visual verification, consisted of inspecting the registered point cloud for point blending (e.g., no single scan color dominated in areas of overlap where the scan worlds had similar point densities), and ensuring the points followed a single profile while looking at cross sections of the registered dataset. Figure 8 shows a top view of the project site. Note each scan position is defined by a different color.

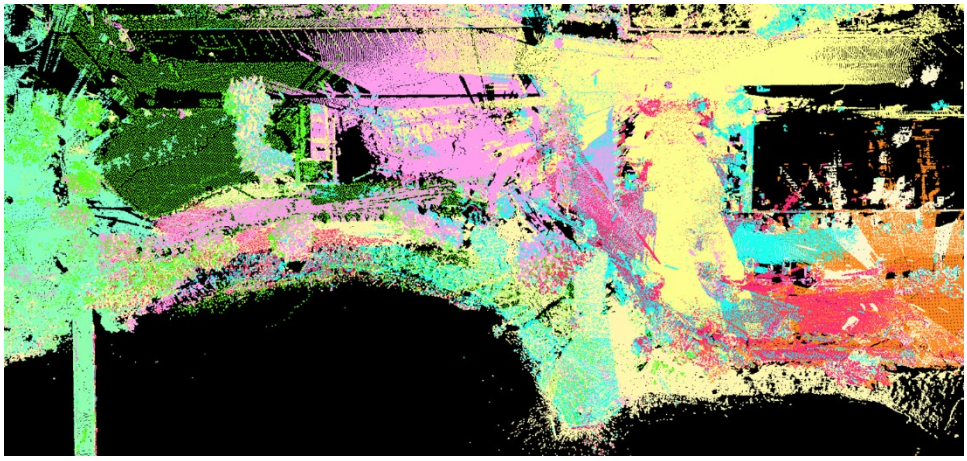

Figure 8: Image showing the top view the AOI with each scan colored differently.

The point cloud classification for this dataset was also completed within Cyclone. To accomplish this task, the point cloud was first thinned, to increase computer hardware performance, at a minimum spacing of 1.0 cm. This process did not include any gridding of the data but simply removed points if the spacing between them was closer than 1.0 cm. This point thinning was primarily located in areas within 35 meters from a scan position. To classify the registered point cloud, 1-5 m cross sections were taken

throughout the entire AOI with points being manually selected and placed in one of the following classification layers: Ground, Noise (high), Noise (low), High Vegetation, Low Vegetation, and Buildings. Figure 9 shows a cross-section of the ground before and after the classification process. After the point cloud had been classified it was exported as a .pts file, later converted to a .las using Cloud Compare (couldcompare.org) to be loaded into QCoherent LP360 (GeoCue Group, Inc.) for further analysis.

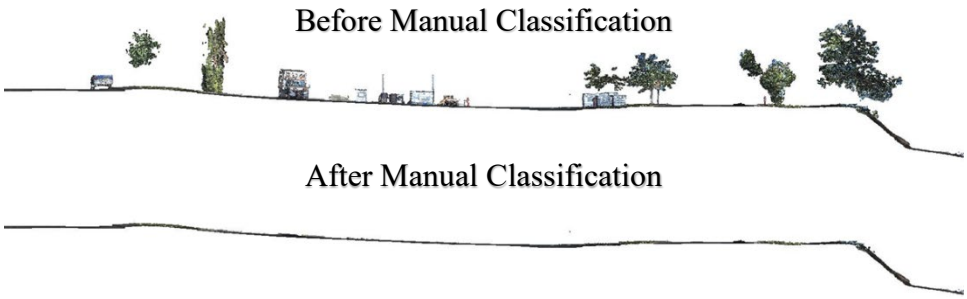

Figure 9: A cross-section of the registered lidar point cloud before (top) and after (bottom) manual ground classification using Leica Cyclone.

2.4 Structure from Motion (UAS)

2.4.1 Structure from Motion Data Collection

A custom DJI s900 hexacopter with PixHawk flight controller was used to collect the aerial imagery which was processed using Agisoft Photoscan SfM software. The aircraft has a maximum takeoff weight of approximately 8.2 kg, allowing it to carry all necessary sensors, including the Sony A6300 camera with Sigma 30mm lens and a Piksi Muli, multi-frequency, GNSS receiver logging at 20 hertz to provide carrier phase-based relative positioning for the collected imagery while maintaining an adequate flight time of 12-15 minutes. All sensors were attached to the aircraft using custom 3D printed parts, which can be identified by their color, orange, in Figure 10. The mount for the Sony A6300 was designed to align the cameras optical axis with the z (down) axis of the aircraft reference frame. The primary justification for using this custom fixed mount as opposed to a 3-axis gimbal is that the lever arms measured from the antenna to the sensor remain approximately constant with respect to the camera reference frame with minimal movement being allowed by the vibration dampeners located on the top section of the

custom mount. It has also been shown that using a wider range of image viewing angles, in combination with precise GNSS positioning, can increase image observations per point resulting in improved survey precision (James, Robson and Smith, 2017). This shows that having nadir imagery is not a requirement when creating 3D models, and, therefore the 3-axis gimbal was not deemed necessary.

Figure 10: The s900 airframe with Piksi Multi GNSS Receiver, GNSS antenna, and Sony A6300 camera with sigma 30mm lens prior to takeoff.

ArduPilot Mission Planner version 1.3.52 was used as the ground station and mission planning software for this flight. The flight was completed as to best replicate parameters typically used in industry, with the controlling parameters being the ground sampling distance (GSD) chosen to be 1.5cm, and overlap/sidelap each set to 80 percent. A screen shot of the planned mission from Mission planner and additional flight parameters are shown in Figure 11 and Table 7 respectively.

Figure 11: The waypoint mission plan used to acquire the aerial imagery as created by ArduPilot's Mission Planner software.

Table 7: A summary of the parameters from the planned mission, as shown in figure 11, used to collect the aerial imagery.

Setting	Value
Area (acres)	8
Flying altitude (ATO) (ft)	377
Sidelap/Overlap (%)	80/80
GSD (cm/pixel)	1.50
Flying Speed (m/s)	5
No. of Photos	163
No. of flight strips	16
Distance Between Lines (m)	18.0
Distance Between Images (m)	12.0
Estimated Flight Time (min:ss)	9:56
Time between triggers (s)	2.39

Special care was taken when setting image acquisition parameters for the camera, including ISO range, shutter speed, aperture, and white balance. All imagery was captured and processed in raw file format. The raw file format maintains all data acquired by the sensor while providing a high dynamic range that can decrease the total area of poorly exposed features in an image. Due to an increased time for the camera to processes the data in raw format compared to .jpg, the flying speed for the mission was

decreased to ensure the time between images was greater than 2.0 seconds. This minimum time between photos when captured in raw format was previously estimated in a lab environment and can vary based on camera make/model, SD card make/model, lighting conditions, and temperature. Note, if the time between images for a planned mission is less than the time required for the camera to process the image there is a chance that image triggers can be delayed, or in some cases skipped resulting in non-uniform overlap/sidelap and/or data voids throughout the dataset. Table 8 contains the camera settings used for acquiring the imagery for the AOI.

Table 8: Summary of the camera settings used for this data collection.

Setting	Value
Camera Make/Model:	Sony A6300
Lens Make/Focal Length:	Sigma 30mm
File format:	RAW (.arw)
Camera Mode:	Manual
Shutter Speed:	1/1250
Aperture:	F5.6
ISO [min, max]	Auto [100, 400]
White Balance	5850k
Focus	Auto (center)

In order to properly georeference the imagery acquired by the Sony A6300 an event is captured by the GNSS receiver when the camera is triggered. This shutter event trigger is sent from the hot shoe flash adapter on the camera to the GNSS receiver as shown in Figure 12. When the camera shutter is opened, a pulse is sent to the GNSS receiver and the time stamp event is recorded for that particular image. The camera positions, and their covariances, for each time stamp plus half of the exposure time were then extracted from the GNSS trajectory using a custom MATLAB algorithm and saved in a comma delimited file structure with the corresponding image file name for import into Agisoft Photoscan.

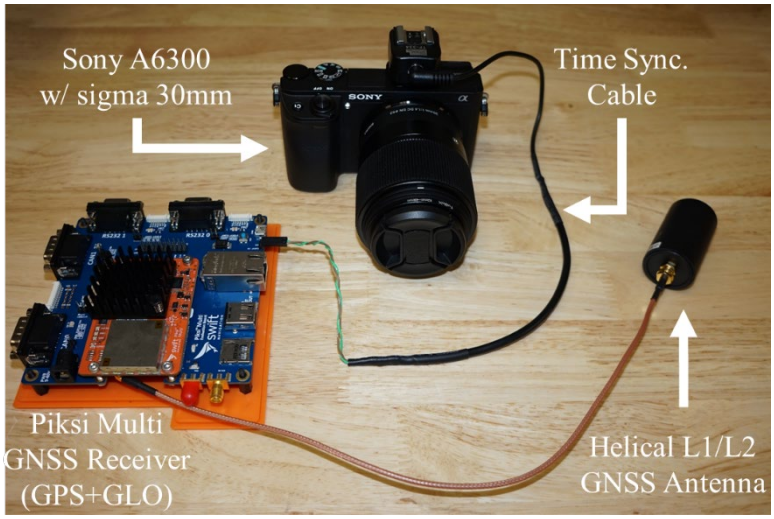

Figure 12: The time synchronization setup used for georeferencing the aerial imagery acquired by the Sony A6300 camera.

2.4.2 Structure from Motion Processing

2.4.2.1 Image Georeferencing

Using the post-processed kinematic GNSS trajectory of the mapping mission reduces the need for ground control points when using Structure from Motion software, thus decreasing the total data acquisition time. The position (X, Y, Z) of each photo is attained from the PPK trajectory and are used to seed the SfM algorithm. These seeded image coordinate values aid the SfM algorithm by constraining the position for each photo, rather than relying on established ground control points, allowing the algorithm to better refine the position (X, Y, Z) through the use of the least squares bundle block adjustment while also determining the remaining extrinsic (roll, pitch, yaw) and intrinsic parameters of the camera.

To georeference the imagery acquired by the Sony A6300 an accurate flight trajectory was calculated from the onboard dual-frequency, carrier-phase GNSS receiver. The Piksi Multi GNSS binary file was converted to raw GNSS observables in RINEX (.obs), and navigation format (.nav) file formats using Sbp2Rinex.exe provided by Swift Navigation. Additionally, the camera trigger timestamps for all images were extracted from the logged binary file using Sbp2Report.exe, also provided by Swift Navigation. Once the

raw binary information was converted to the necessary formats, the aircraft trajectory was calculated and the acquired imagery was ready to be geotagged. The overall workflow for geotagging the imagery is shown in the flow chart, Figure 13.

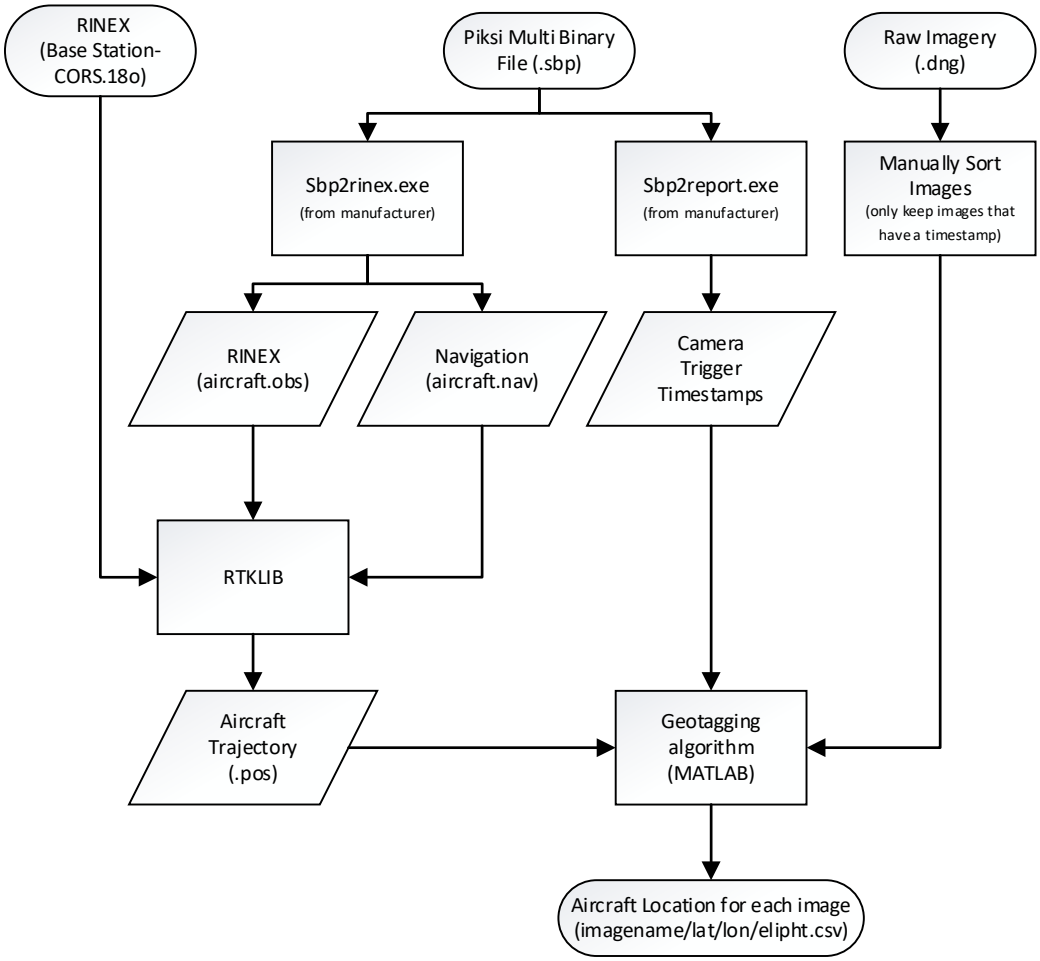

Figure 13: A summary of the workflow used to georeference the aerial imagery.

The open-source GNSS processing software package, RTKLIB (Takasu and Yasuda, 2009), was used in post processing kinematic (PPK) positioning mode to compute the remote aircraft's trajectory. The following data for the acquisition date was downloaded from various sources: RINEX file from a continually operating reference station (CORS) located approximately 1.8 kilometers from the AOI, the precise ephemeris, and the satellite and station clock solution. After processing the trajectory, it was found that RTKLIB v2.4.2 was unable to solve for the integer ambiguities for GLONASS satellites.

Hence, the resulting trajectory was a GPS only L1/L2 solution with an average satellite vehicle (SV) count of 8. RTKLIB beta version 2.4.3 demo5 b29c (Everett, 2018), a modified version of 2.4.3 b29c for the improvement of GLONASS support, was also tested to see if this would improve the trajectory. Table 9 outlines the settings used in both versions of RTKLIB to process the trajectory. Note the processing settings for the two versions only differed for the integer ambiguity resolution for GLONASS parameter. The newer version of RTKLIB resulted in a trajectory solution that utilized both GPS and GLONASS with an average satellite vehicle count of 15.

Table 9: A list of the non-default processing settings used in RTKLIB 2.4.2

Setting	Value
Constellations Used:	GPS, GLONASS
Frequencies:	L1/L2
Ionosphere Correction:	Broadcast
Troposphere Correction:	Saastamoinen
Satellite Ephemeris/Clock:	Precise
Integer Ambiguity Resolution: GPS/GLO	Continuous/ON (v2.4.2) Continuous/Fix&Hold (v2.4.3 demo 5)

Lastly, to geotag the acquired imagery, both the processed trajectories and image time stamps were imported into a custom MATLAB script that determines the position for all images (latitude, longitude, ellipsoid height), and their covariances as produced by RTKLIB, for each time stamp plus one half of the exposure time. This addition of half the exposure time allowed the position to be extracted at approximately mid exposure, which is the ideal location to geotag the image (Turner, Lucieer and Wallace, 2014). Once the positions are extracted for each camera from the GNSS trajectory, they are saved in a comma delimited file structure with their corresponding image file name. After the file was exported the coordinates were transformed to the correct horizontal and vertical reference systems. To transform the horizontal coordinates from NAD83(2011) latitude and longitude to Washington State Plane South (4602) in meters NOAA NGS Coordinate Conversion and Transformation Tool (NCAT) was used. NOAA's VDatum (v3.8) was then used to transform the vertical coordinates from NAD83 elliposoid heights

to NAVD88 orthometric heights utilizing Geoid 12B. Once these transformations were applied, the trajectory was ready for import into Agisoft Photoscan. Note that no lever arms or offsets were applied to this trajectory. Therefore, the trajectory is the position of the phase center of the GNSS antenna. The lever arms from the phase center to the nodal point of the camera in respect to the cameras reference frame, as defined by Agisoft Photoscan, had been previously determined in Agisoft using a calibration flight with a dense control network. This method to attain the lever arm measurements was chosen because attaining accurate manual measurements to the poorly defined camera nodal point and antenna phase center can prove to be difficult.

2.4.2.2 Agisoft Photoscan

Because there were multiple datasets processed with varying constraints (satellite constellations used, and number of control points), a processing outline was used in order to ensure consistency between the datasets. In order to properly utilize the image coordinates acquired from the PPK GNSS trajectory the lever arm measurements, with respect to the camera local reference frame, were input into Agisoft Photoscan. In this case, because no antenna model or offsets were applied to trajectory during processing, the lever arms are measured from the nodal point of the camera to the phase center of the GNSS antenna with respect to the sensor reference frame. The sensor reference frame, as established by Agisoft, is described as follows when the camera is oriented in the nadir direction (lens point straight down) with the top of the camera (i.e. the hot-shoe of the A6300) pointing forward:

- +X is to the right (for the A6300, towards the cameras handle)
- +Y is forward (towards the top of the camera i.e. the hot-shoe)
- +Z is straight up, or zenith (if looking through the eye piece of the camera this would be into your eye)

Because of the image georeferencing only a few control points were utilized to help correct for any systematic errors in the position of the resulting 3D model. Therefore, only one or five of the control points were activated for any particular dataset, leaving the remaining control points to be utilized as check points. Figure 14 shows an orthomosaic

identifying the point ID and location for each of the control point(s) used. For datasets for which only one control point was used, the aerial target located nearest to the center of the AOI was used; Point ID A54. For the datasets utilizing 5 control points the aerial targets located nearest to the four corners of the AOI, and the center point was used; A12, A19, A23, A52, and A54.

Figure 14: The five control points used for the the SfM processing. For datasets where only one control point was used the aerial target located nearest to the center of the AOI was used; Point ID A54. For the datasets utilizing 5 control points the aerial targets located nearest to the four corners of the AOI, and the center point was used; A12, A19, A23, A52, and A54

Ground points were then classified utilizing the Classify Ground Points tool within Agisoft Photoscan. After the initial classification was completed a quality assurance check was conducted to ensure the resulting ground points were classified correctly. This required a fair amount of manual point classification in areas of dense vegetation, and areas where the ground slope was greater than 15 degrees.

This processing methodology was used to create four different models: (i) 1 control point with GPS & GLONASS trajectory; (ii) 1 control point with GPS only trajectory; (iii) 5 control point with GPS & GLONASS trajectory; (iv) 1 control point with GPS only trajectory. To reduce the introduction of user errors or biases the models using 5 control points were created using the initial alignment created for the models with 1 control point.

2.4.2.3 Grid Ground Points

One of the primary products derived from SfM-MVS processing is the dense point cloud. An issue is that this dense point cloud can sometimes be so dense that it can be overly demanding for current lidar point cloud processing software suites that were primarily developed for working aerial lidar data from manned aircraft, which typically have much lower point densities. In addition to this larger demand there is also a substantial amount of noise in the data. To help reduce this noise and decrease the overall point density, a binning algorithm was implemented in MATLAB. Using this binning algorithm the exported .las file from Agisoft was read in and binned into user specified grid cell sizes. In this case, a 5cm grid was used to ensure there were enough points to produce confident statistical values without over smoothing, or removing, vertical features from the dataset. This grid cell size also corresponded well with the average point spacing from the UAS based lidar mission, which resulted in a point spacing of ~5cm. After the data was binned statistics (mean, median, number of points, variance from the mean, standard deviation, minimum, and maximum) were computed for the Z values of the points within these cells. Displaying color-ramped raster images of these statistics also facilitated visual assessment of the spatial variation in noise throughout the dataset. For the comparison between various different acquisition equipment, the median value for the bins will be used as it does the best job at not being influenced by outliers in each bin that would typically affect the mean more drastically.

2.5 Aerial Lidar (UAS)

2.5.1 Aerial Lidar Data Collection

The UAS-lidar data was collected using a Phoenix Lidar System AL3-32 integrated Lidar-INS system comprised of a Velodyne HDL-32E lidar sensor and NovAtel KVH1725 GNSS aided inertial navigation system (INS) mounted on a DJI M600 Pro UAS with an A3 flight controller (Figure 15) by local survey firm, Klein and Associates, located in Hood River, Oregon. The mission flight plan was created using Phoenix Aerial Systems SpatialExplorer ground station program which also creates a real time, typically less accurate than post processed, display of the acquired data. The system was flown at

180 feet above ground level (AGL) emitting pulses at a rate of 695 kHz with a scan angle in the direction of travel ranging from 30.67° forward from nadir and 10.67° backward from nadir, for a total field of view equal to 41.34°.

Figure 15: The Phoenix Aerial al3-32 Scanner mounted on a DJI m600 Pro. Image courtesy of Phoenix Lidar Systems, https://www.phoenixlidar.com/al3-32/

The acquisition settings were developed to yield points with a native density greater than 150 pulses per square meter. Note, the native pulse density is the number of pulses emitted from the scanner, whereas, the delivered pulse density is the number of pulses returned to the sensor. Surfaces such as dense vegetation, water, etc. commonly return fewer pulses than the sensor emitted, but this decrease in pulse returns can be remediated by the sensor's ability to acquire dual returns per pulse. To solve for the laser point position it is crucial to have highly accurate observations of the sensors position (X, Y, Z) and attitude (Roll, Pitch, Yaw). The GNSS was set to log at 1 Hz, while the IMU logged inertial sensor measurements at 200 Hz. The GNSS base station was located approximately 0.1 km from the center of the AOI. Overall, there were a total of 20 flight lines used to acquire the data over the AOI as shown in Figure 16.

Figure 16: An image of the 20 flight lights used for acquiring the aerial lidar dataset.

2.5.2 Aerial Lidar Processing

For processing the aerial lidar data three different software suites were utilized: NovAtel's Inertial Explorer™, Phoenix Aerial Systems SpatialFuser, and TerraSolid's TerraScan/TerraMatch which is built on top of Bentleys' CAD software, MicroStation.

NovAtel's Interial Explorer is used to iteratively refine the measured lever arms from the IMU reference frame origin to the GNSS antenna phase center until the values coalesced. After the lever arms are refined, the trajectory measured from the GNSS aided INS is recomputed and exported in SBET (smoothed best estimate trajectory) file format. The final trajectory was then imported into Phoenix Aerial's proprietary software, SpatialFuser, which is used to combine time synchronized laser observations, with the SBET to create the 3D point cloud. Specific details of the software are company-proprietary, but the general procedure likely follows the following basic steps:

1. Apply approximate boresight between lidar sensor origin and GNSS aided INS origin
2. Interpolate position (X, Y, Z) and attitude (roll, pitch, heading) from the trajectory for all lidar returns
3. Apply geolocation equations, which include transforming 3D coordinates from the laser scanner frame to the INS frame, local level frame, earth centered earth fixed (ECEF) frame, and finally to the specified mapping frame
4. Export georeferenced point cloud

After the 3D point cloud has been generated it is refined using TerraSolid's TerraMatch software. TerraMatch is primarily used to maximize relative accuracy between flight lines by refining boresight values and accounting for changes in the measured lever arms. To refine the boresight values the software solves for global, flight line, and fluctuation corrections for the position and attitude of all flight lines. These corrections are then applied to the trajectory to maximize the relative accuracy of the various flight lines. As a result of this process, a more seamless data set is achieved, because the systematic orientation and position errors have been largely removed. To increase the global accuracy, a single control point taken on a horizontal, flat, and hard surface at the center of the AOI, was used to apply a vertical offset to the data to alleviate any offsets caused by random or systematic errors remaining in the data set.

Once the georeferencing of the point cloud was completed, an automated point classification algorithm was implemented within TerraScan to create the following classification fields: ground, low/medium/high vegetation, buildings, low/high noise, and water. Finally the point cloud was colorized by applying RGB values to each point from an overlaid orthophoto created using co-acquired RGB imagery.

2.6 Vertical Accuracy Assessment

The most common metric for comparing various 3D data is by comparing their spatial accuracies. Therefore, the vertical accuracy of the various processed datasets were computed using the reference data acquired in the control survey. A summary of the datasets being analyzed are shown in Table 10. For the vertical accuracy assessment the

reference data was separated into 3 categories based on surface type: asphalt, bare earth and grass; quantities are summarized in Table 11. Each of these vertical check points were collected in accordance with ASPRS vertical checkpoint density and accuracy standards. These standards specify that checkpoints should be surveyed on flat uniformly-sloped open terrain away from abrupt changes in elevation, with slopes of 10% or less. Additionally, these standards require a minimum number of 20 checkpoints for each surface type distributed evenly throughout the mapping area when possible (American Society for Photogrammetry and Remote Sensing, 2014).

Table 10: Summary of the processed datasets to be compared using the numerous, unobstructed, vertical check points.

Dataset	Sub-dataset	Total number of datasets
Terrestrial Lidar	N/A	1
Aerial Lidar	N/A	1
SfM – 1 CP – GPS Only	Median of Bin, Raw	2
SfM – 1 GCP – GPS+GLO	Median of Bin, Raw	2
SfM – 5 CP – GPS Only	Median of Bin, Raw	2
SfM – 5 GCP – GPS+GLO	Median of Bin, Raw	2
	Total:	**10**

Table 11: Summary of the quantities of the unobstructed control points being used for the vertical accuracy analysis.

Surface Type	Quantity
Asphalt	43
Bare Earth	32
Grass	25

The vertical analysis was completed empirically using QCoherent LP360. This assessment is accomplished by comparing the point cloud data sets against the reference control, often referred to as “ground truth.” To do this assessment LP360 first creates a triangulated irregular network (TIN) for each point cloud and then computes a point-to-TIN offset, in the vertical direction only, for each control point. After these offset values

are determined, summary stats such as mean, median, range, standard deviation, and $RMSE_z$ are calculated and compared.

3 Results and Discussion

3.1 Point Cloud Properties/Characteristics

The progress in miniaturizing INSs and lidar systems onto UAS platforms is relatively new, but the basic methodology and limitations of UAS-lidar are comparable to traditional airborne lidar from manned aircraft. SfM-MVS applications for topographical mapping has more recently been developed for implementation in industry. This research indicates that UAS-SfM is capable of providing satisfactory topographic mapping results with a simple, user friendly, acquisition and processing interface. The average point density and point spacing of each of the point clouds were calculated using LP360 point density tool. Table 10 summarizes these densities, showing that UAS-SfM is capable of providing greater density when compared to UAS-Lidar. UAS-SfM does provide many advantages over UAS-Lidar, but it is less robust to the operating environment, and there are specific cases in which it can fail.

Table 12: A summary of the average point density and spacing for the point clouds being compared.

Point Cloud	Average Point Density (pts/m^2)	Average Point Spacing (cm)
Terrestrial lidar (reference data set)	7000	1.2
UAS-lidar	50	14.5
UAS-SfM raw	5500	1.3
UAS-SfM grid	350	5.4

The results enabled an analysis of the specific conditions that impacted the quality of the SfM results. For example, the output of the binning algorithm implemented on the SfM raw dense point cloud (ground only) enabled extraction of statistical information (mean, median, number of points, variance from the mean, standard deviation, minimum, and maximum) for each of the 5 cm × 5 cm square bins, which contained an average of 24 points per bin. Figure 17 contains an orthomosaic image of the AOI (top), and the

resulting binned point cloud, bottom, colored by standard deviation from the mean where blue indicates a standard deviation of 0.00 centimeters and yellow a value of 0.10 centimeters. Visualizing the point cloud by standard deviation allows for easily identifying areas containing increased noise in the data. These areas of increased noise help determine what specific site conditions lead to less reliable surface reconstructions. Visual analysis reveals that areas of high standard deviation in Figure 17, identified by the dashed rectangles, generally correspond to areas with a combination of poor texture and a decrease in overlap/sidelap, due to being on the edge of the flight plan and being surrounded by large vertical objects (trees and/or buildings). Similarly, the higher standard deviations in the dashed ovals correspond to a combination of homogenous texture, poor lighting, and increase in camera obstructions.

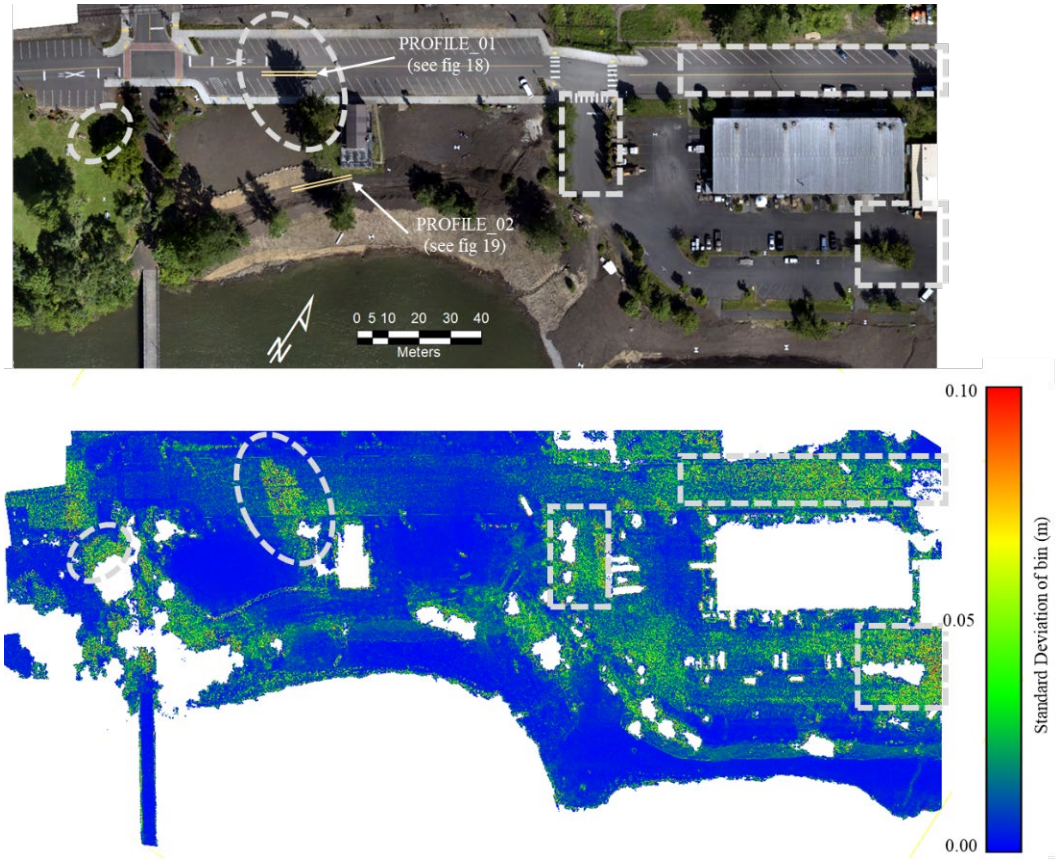

Figure 17: Includes the orthophoto created within Agisoft photoscan (top), and the standard deviation of the points within each 5 cm bin used to grid the resulting SfM point cloud data. The point cloud is colored with 0.0 meter standard deviation in blue and a 0.1 meter standard deviation in red. The selected area identified by the light dashed lines on the images indicate areas with higher standard deviations, or noise, in the data.

This analysis provides insight into the effects of poor illumination and of low texture, both individually and in combination. Detailed cross sections of two areas being shadowed by nearby trees are shown in Figure 18 and Figure 19. The first cross section shown in Figure 18 is of asphalt, a low texture surface, where the combination of poor texture and poor lighting conditions resulted in an increase in noise for the SfM data set compared to the lidar data sets that showed no change. The second cross section, shown in Figure 19, is of an area of bare earth, a higher texture surface. In this case, the higher texture was sufficient to overcome the challenges of poor illumination. This suggests that it is the combination of low texture and poor illumination that poses the greatest challenge.

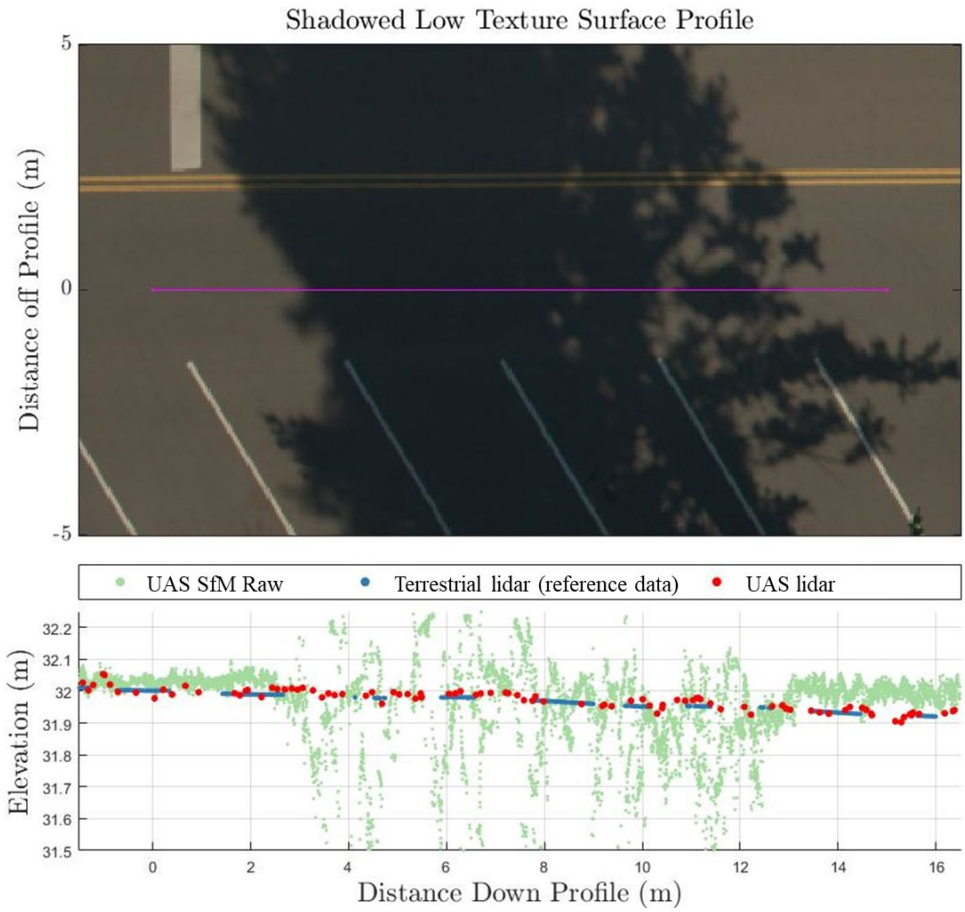

Figure 18: Top view of a shaded segment of asphalt (top) with a profile that intersects the shaded region (bottom). This is a prime example of the downside of using a passive sensor as the poor lighting can lead to a decrease in captured texture, thus increasing noise in SfM processed data sets.

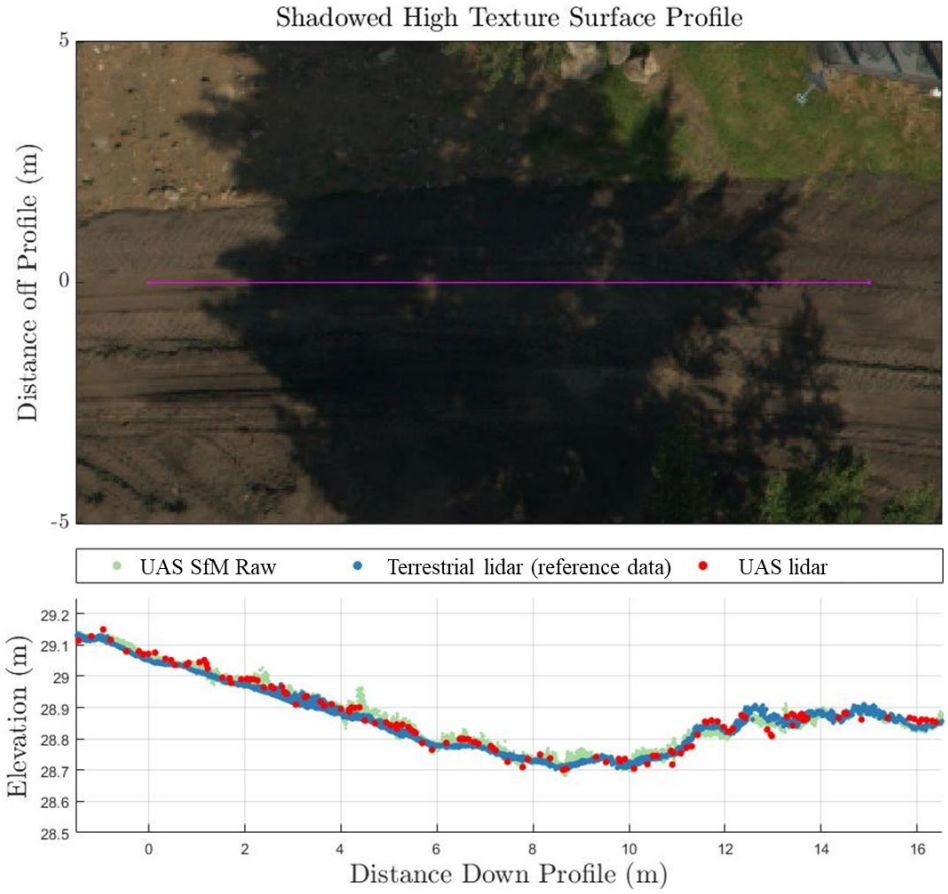

Figure 19: Top view of a shaded segment of bare earth (top) with a profile that intersects the shaded region (bottom). This is an example that depicts that some surfaces are not impacted by the poor lighting conditions and are able to maintain adequate texture for accurate surface reconstruction when compared to active sensors such as terrestrial and drone based lidar.

In order to compare the performance of aerial drone-based lidar to drone-based SfM, a cross section was taken, shown in Figure 20, for each of the main surface types: asphalt (top), bare earth (middle), and grass (bottom). Each of the cross sections contains the following datasets: SfM Raw, which is the SfM point cloud prior to being gridded; the median of the gridded SfM point cloud; the terrestrial lidar point cloud, the aerial drone-based lidar; and the points from the control survey being considered the “ground truth” identified as triangles. Note each profile also has a close-up image of the corresponding surface type to help identify the level of surface texture.

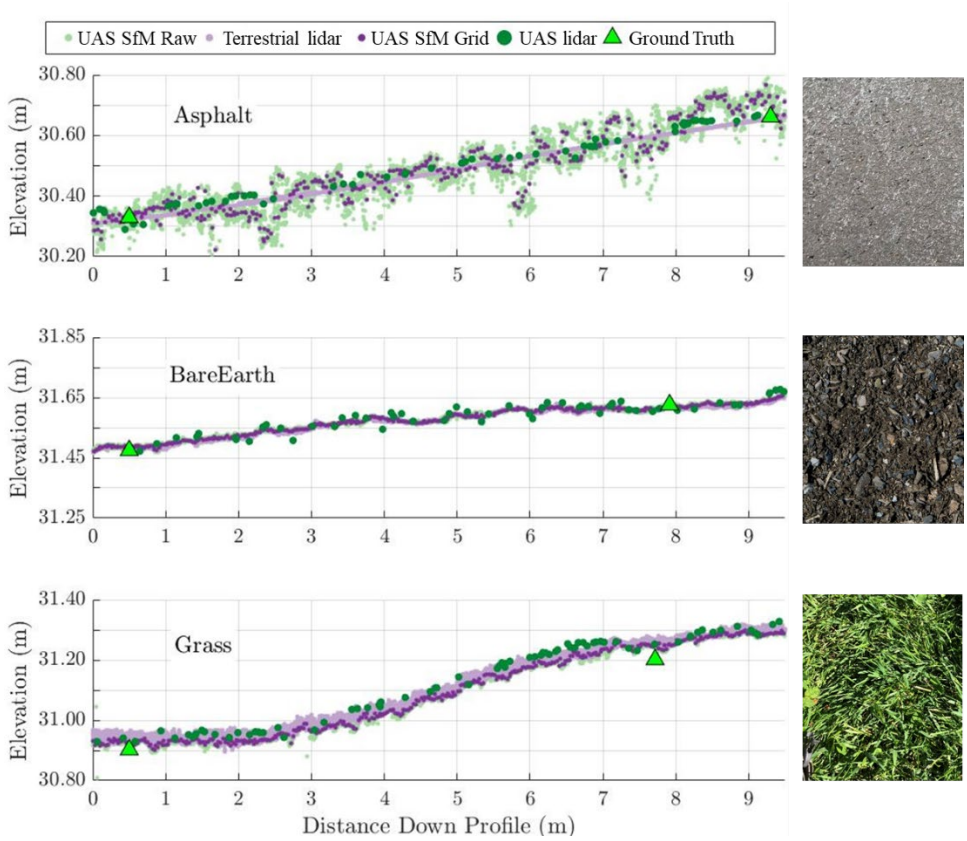

Figure 20: A plot of three profiles for varying surface types, with images of each corresponding surface to the right. Each cross section includes the following data sets: SfM raw (not gridded), terrestrial lidar, SfM median of bins after being gridded at 5cm, aerial lidar, and ground truth points from the control survey.

The raw SfM data set on the asphalt has greater noise when compared to the bare earth and grass profiles shown in Figure 20. This increased noise corresponds to the relatively poor surface texture of the asphalt. After computing the median of the gridded data, the surface is smoothed, reducing the overall noise, but the results are still, in general, worse than the UAS-based lidar for this surface type. Comparing the UAS-lidar to the terrestrial lidar in this profile clearly shows that the UAS-lidar does deviate from the terrestrial data. Looking at the high textured bare earth profile, there are almost indistinguishable differences between the terrestrial lidar and SfM datasets when inspecting them at this level of detail, whereas the UAS-lidar deviates from the terrestrial lidar similarly to the asphalt profile. Inspecting the grass profile, it is apparent that all of the point clouds are higher than the ground truth points collected through the control survey. The majority of

these offsets are inherently due to the height of the grass where the control was observed at the base of the grass and the point cloud observations would be of the top of the grass, as none of the methods would have been capable of penetrating through the dense vegetation.

3.2 Vertical Accuracy Analysis

Before comparing the accuracy of UAS-SfM to UAS-lidar a comparison between the various UAS-SfM datasets was first completed. The UAS-SfM assessment compares the effects of using a GPS only PPK trajectory versus a GNSS PPK trajectory used to geotag each image. It also includes a brief GCP sensitivity comparison to determine the overall impact of utilizing more GCPs has when the imagery is precisely georeferenced. Note, as described in section 2.6, the check points acquired in the control survey are being used as the referenced control dataset. The results of this analysis are summarized in the plots in Figures 22-24. In each plot, five different elevation data products generated using different processing procedures are assessed by comparison against total station reference data acquired from the control survey: 1) terrestrial lidar (solid orange bars); 2) median filtered UAS-SfM with 1 ground control point using GPS only (solid red bars); 3) median filtered UAS-SfM with 1 ground control point using GPS+GLONASS (cross-hatched red bars); 4) median filtered UAS-SfM with 5 ground control points using GPS only (solid blue bars); and 5 median filtered UAS-SfM with 5 ground control points using GPS+GLONASS (cross-hatched blue bars). The results of these comparisons were first expressed in terms of vertical accuracy at the 95% confidence level, computed as $1.96 \cdot RMSE_Z$, following FGDC's *National Standards for Spatial Data Accuracy* (FGDC, 1998):

$$RMSE_Z = \sqrt{\frac{\sum_{i=1}^{n}\left(Z_{data_i} - Z_{check_i}\right)^2}{n}} \tag{4}$$

Next, the comparison results were decomposed into a mean (or bias) and standard deviation about the mean. This breakdown is helpful to gain insight into whether the differences between the total station reference data and various elevation data sets are

dominated by a large systematic error (bias), or are more indicative of a large random uncertainty. Note that for large n, the following relationship between the *RMSE*, the mean, μ, and the standard deviation, σ, is expected to hold (Stewart *et al.*, 2009):

$$RMSE_Z^2 \approx \mu^2 + \sigma^2 \tag{5}$$

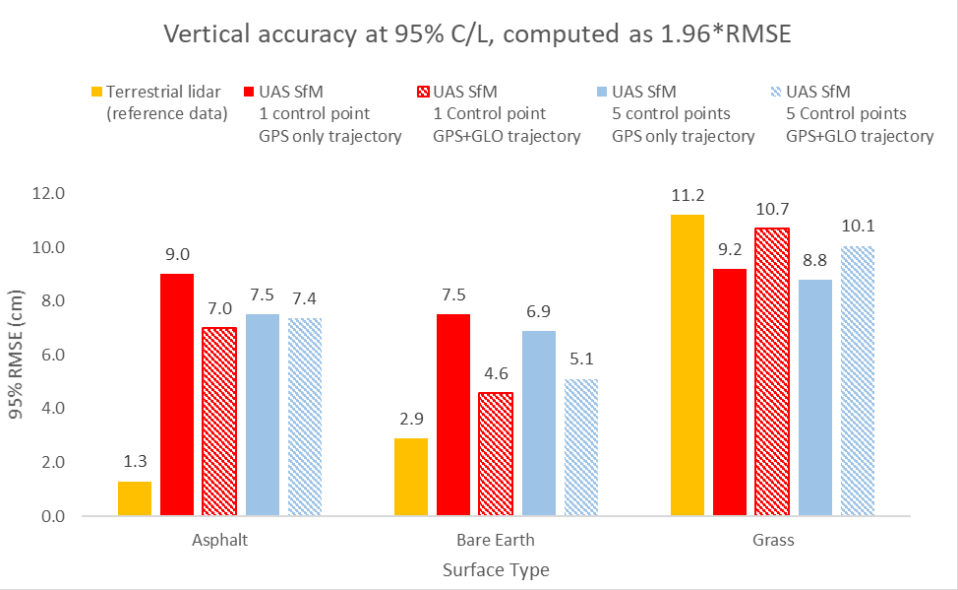

Figure 21: Vertical accuracy at 95% confidence level (computed as 1.96*RMSEz) from comparison of each of the 5 elevation data sets against the reference total station data

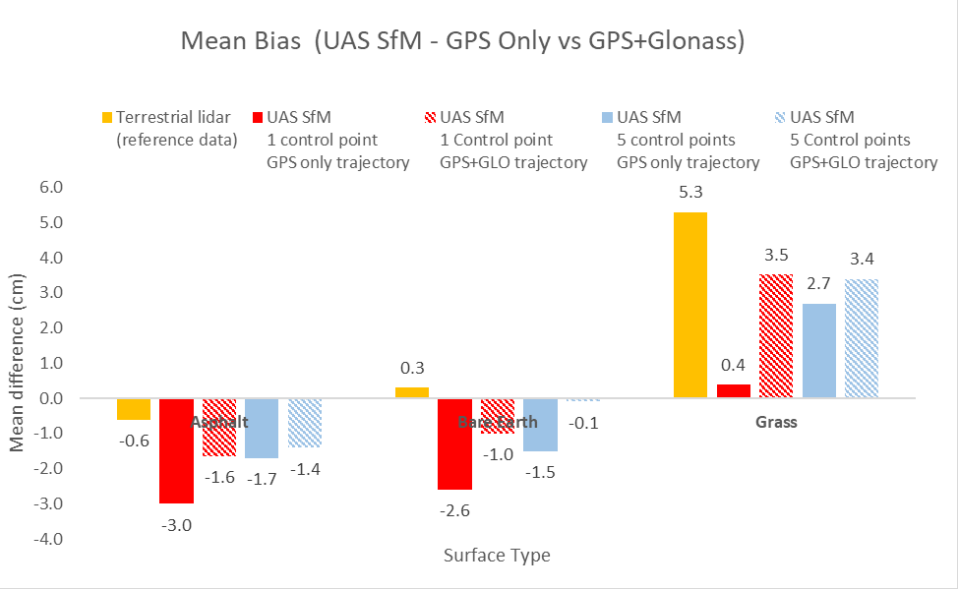

Figure 22: Mean difference (bias) from comparison of each of the 5 elevation data sets against the reference total station data.

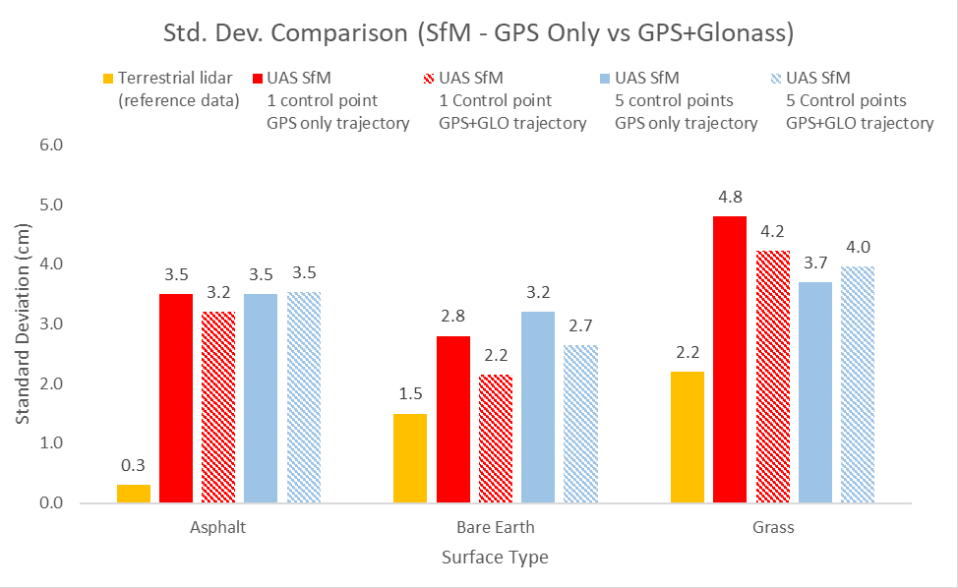

Figure 23: Standard deviation about the mean from comparison of each of the 5 elevation data sets against the reference total station data.

The following general observations can be made from Figures 22-24:

1. In grass, the terrestrial lidar data exhibits a larger bias, attributable to the depth of the grass (~5cm from the surface of the grass to the ground where the control was

measured) and poor viewing geometry to penetrate the top surface of the vegetation, compared to the SfM data sets which have a more nadir viewing geometry allowing for more surface penetration.

2. The results of including GLONASS for georeferencing the imagery were mixed: sometimes GLONASS helped, and other times, it did not. But it did typically provide a solution closer to the terrestrial lidar results.
3. When using accurate georeferenced imagery the inclusion of more control (i.e. 5 control points (blue) vs. 1 control point (red)) did not have a large influence when comparing the standard deviation, but it did reduce the bias on hard surfaces.

The next step in the analysis consisted of examining three different acquisition systems: 1) SfM-MVS processing of drone-based imagery after a median filter has been applied, 2) airborne, drone-based lidar, and 3) terrestrial lidar for reference. The results of this analysis are summarized in Figures 25-27. Once again, the results are summarized first in terms of accuracy at the 95% confidence level, followed by a decomposition into a mean (bias) and standard deviation about the mean.

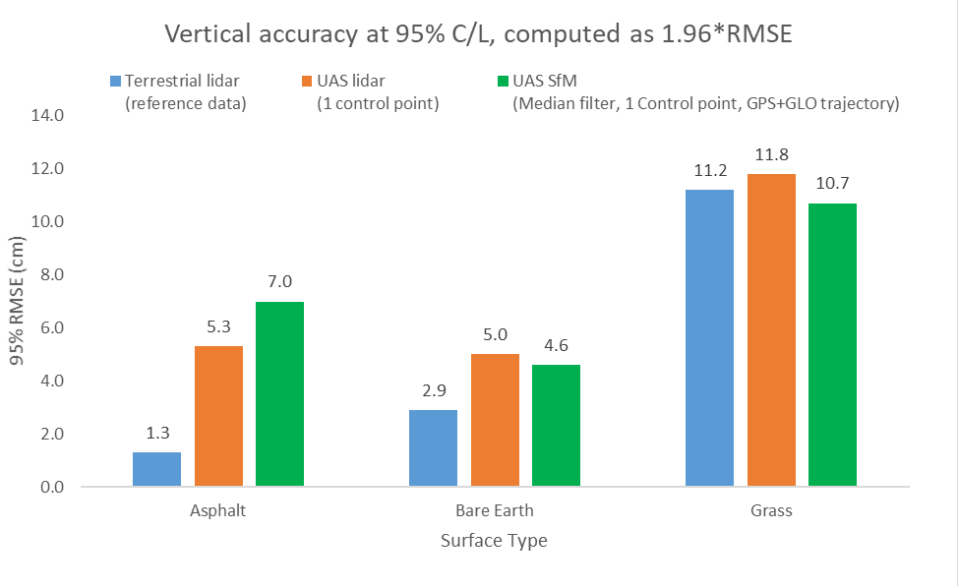

Figure 24: Vertical accuracy at 95% confidence level (computed as 1.96*RMSEz) from comparison of each of the 3 primary comparison elevation data sets against the reference total station data.

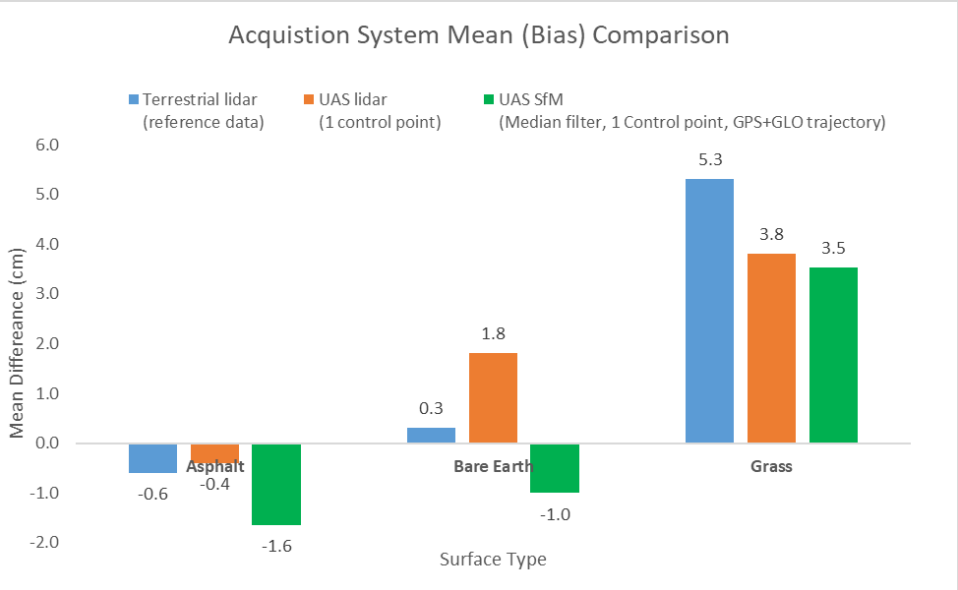

Figure 25: Mean difference (bias) from comparison of each of the 3 primary comparison elevation data sets against the reference total station data.

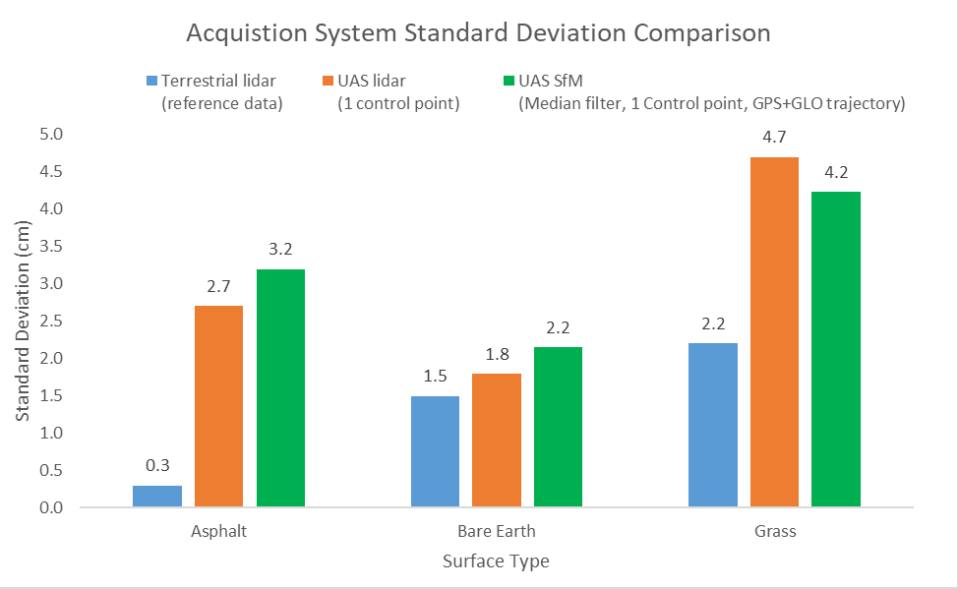

Figure 26: Standard deviation about the mean from comparison of each of the 3 primary comparison elevation data sets against the reference total station data.

Analysis of Figures 25-27 leads to the following observations:

1. Drone-based SfM or lidar is not nearly as accurate to terrestrial lidar on hard, flat surfaces (asphalt or bare earth), but both perform similarly to, if not better than, terrestrial lidar over grass. This similarity over grass is expected as the grass is a very dense vegetation, making it difficult for all platforms to consistently observe to the ground surface. However, because of the viewing geometry of the airborne systems, they are able to penetrate down into the vegetation slightly, resulting in a decreased bias to the ground truth. The increase in standard deviation over the grass seen for both aerial platforms is most likely attributed to the variability of the grass density which affects how deep into the vegetation the sensors can see (UAS-SfM) or penetrate (UAS-lidar) at each checkpoint.
2. Relatively small differences in accuracy are observed between drone-based SfM and drone-based lidar for all surface types using these specific sensors and acquisition parameters.

3.3 Synthesis and Discussion of Results

3.3.1 Overall Benefits and Limitations

The primary difference between the two mapping techniques compared in this paper is that UAS-lidar is an active sensor, and UAS-SfM is based on data acquired from a passive sensor. The passive sensors are inherently susceptible to the lighting conditions of the area of interest, and, as a result, the final product can be greatly impacted, as shown in the example areas containing poor lighting caused by tree shadows. This limitation has a hindrance on acquisition times and/or locations when compared to aerial lidar, an active sensor. For example, it would be very difficult to collect reliable data for SfM processing at night, whereas an active sensor should not have any difficulty (assuming, of course, that it is possible to obtain an FAA waiver for nighttime operations). Another major limitation to SfM processing is that it requires that the surfaces being reconstructed are well as textured in order for the algorithm to function correctly. This paper has shown that on surfaces with high texture, such as bare earth in

this case, the accuracy of the reconstructed model is comparable to the UAS-lidar. Conversely, the model would have a decreased accuracy and a high standard deviation, or noise, on surfaces with low texture (e.g. asphalt).

UAS-lidar primarily excels due to its low dependence on lighting and surface conditions. Unfortunately, typical drone based lidar systems have much greater cost than a typical SfM mapping platform, due to the intricate suite of costly sensors such as the lidar scanner, and the GNSS-aided INS. This increase in equipment cost might be justified, especially if the areas being mapped are not well suited to SfM processing. For example UAS-lidar would be more suitable in areas with poor illumination, thick canopy cover/vegetation and/or homogenous surface textures. Additionally, UAS-lidar is capable of providing point return intensities, which can be used to identify various surface characteristics. Although lidar point clouds can be colorized by RGB similar to the SfM derived points clouds, the technique used to colorize the lidar point clouds can be subject to parallax, leading to positional uncertainties in the RGB values. This is because the lidar is colorized by overlaying a co-acquired orthomosaic image over the resulting point cloud. Therefore, care should be taken when identifying items based on RGB color as opposed to intensity as any positional uncertainties in the orthomosaic image can result in a color shift on the point cloud. For that reason, in many cases, the derived products from UAS-SfM can be even more useful for surface characterization than UAS-lidar.

The overall quality of the products generated from both mapping platforms discussed in this report relies heavily on the acquisition and processing procedures implemented. Therefore, in order to create accurate and precise final products from the UAS mapping technologies discussed, it is necessary to take notice of the procedures implemented during data acquisition and processing. The UAS-lidar data set used in this paper was acquired using typical acquisition scanning rates, flying height, and speeds. The acquisition parameters produced a point cloud less dense than preferred, resulting in the inability to accurately extract the center of the aerial control targets. This point density was noticeably decreased over dark surfaces such as the asphalt. In particular, these density artifacts could be corrected for by decreasing the flying altitude and speed, or

increasing the sidelap during data acquisition. Additionally, this paper has proven that using a median filter is an effective method for thinning the dense point cloud from the UAS-SfM data to a more manageable dataset as well as slightly increasing the accuracy of the model, as outliers of a surface are inherently ignored through the filtering process. Note that the median filter should be used with caution as it is possible that the filter can remove small vertical features from the data as a result of this smoothing effect. Table 13 provides an overview of the primary advantages and disadvantages of each mapping platform in order to aid with decision making on which platform should be used for a particular project.

Table 13: An overview of the advantages and disadvantages of each of the 3D point cloud acquisition techniques discussed in this paper as well as terrestrial lidar for reference purposes.

	UAS-Lidar (directly georeferenced)	**UAS-SfM (w/ geotagged imagery)**
Advantages:	– Fast data acquisition time – Provides specific surface characteristics using return strength (intensity) – Active sensor – Able to penetrate tree canopies/vegetation – Captures vertical features – Capable of good global accuracy (less than terrestrial lidar data)	– Fast data acquisition time – Provides very dense 3D data – Low Cost – Simple acquisition system – Relatively Simple Processing Methodology – Capable of good global accuracy (comparable to drone based aerial lidar data)
Disadvantages:	– Processing requires more expertise – Higher cost – Poor return strength on dark surfaces (must limit acquisition altitude) – Complex positioning system required. (GNSS-aided INS) – Typically more sparse 3D data when compared to terrestrial lidar and SfM-MVS derived point clouds	– Does not capture vertical features well when only nadir imagery is used – Passive sensor – Susceptible to increased noise in low texture areas – Unable to penetrate dense vegetation – Heavily reliant on computer processing resources

3.3.2 Summary of Comparison

This study has demonstrated how two common drone mapping techniques used to create dense 3D point clouds, drone-based lidar and structure from motion photogrammetry, compare to each other when referenced and compared against two control data sets: sparse high accurate check points and terrestrial lidar. The overall goal of this research is to provide information to industry surveyors and mapping professionals about the limitations of each of the two mapping techniques. Although the two drone-based techniques are typically less accurate and precise than the well tested and used terrestrial lidar, their ability to collect copious amounts of data by covering larger areas in relatively little time, when compared to traditional surveying and terrestrial lidar techniques, makes them very cost effective when the higher order of accuracy is not required. This cost benefit is especially significant when UAS-SfM is being implemented, as a consumer level, off the shelf, SfM mapping platform with accurate image georeferencing has a relatively low equipment cost when compared to a UAS-lidar system.

The two primary mapping techniques being compared both require the same level of data collection efforts. This ease of data collection for both techniques is largely attributable to their ability to georeference the data, thus eliminating the need for a control survey. For the drone-based lidar this georeferencing is accomplished by directly measuring the position and attitude of the sensor using the onboard GNSS-aided INS system and applying a boresight correction to the lidar measurements. Similarly, for UAS-SfM, the position (X, Y, Z) of each photo is attained through the use of an onboard dual-frequency GNSS receiver and PPK processing to seed the SfM algorithm. This seeded value for the position aids the SfM algorithm by constraining the position for each photo, rather than relying on established ground control points, allowing the algorithm to better refine the position (X, Y, Z) through the use of the least squares bundle block adjustment while also determining the remaining extrinsic parameters (roll, pitch, yaw) and intrinsic parameters of the camera.

Even though the data from both platforms are “directly” georeferenced, constant biases (typically in elevation) may remain in the derived model. To increase the accuracy of the

resulting model, it is tremendously beneficial to establish control points on surfaces throughout the scene. These control points can then be leveraged to perform coordinate shifts on the dataset, thus, alleviating systematic errors, or biases. Setting control targets for aerial mapping missions, especially for UAS-SfM, is time consuming and not cost effective. For this reason, industry has been migrating towards the implementation of PPK/RTK positioning for image georeferencing on UAS-SfM platforms. That said, the inclusion of more ground control points will aid in removing systematic and/or random errors in the final product. As shown in section 3.2, the results from comparing the SfM product derived from using 1 control point versus 5 control points showed little effect on the standard deviation but the additional control points did help reduce the bias between the resulting point cloud and the reference checkpoints.

Although the data collection efforts for UAS-lidar and UAS-SfM are similar, the processing requirements for the two techniques differ greatly. The UAS-lidar processing methodology can require multiple software packages to attain the final product, resulting in a decrease in the general usability. Overall, both methods compared well to the numerous checkpoints used on the various surface types, i.e. grass, bare earth, and asphalt, although it has been noted they each have scenarios where they do not achieve the same level of accuracy and detail as terrestrial lidar, a proven and well trusted 3D data acquisition technique. While Table 13 concisely summarizes the relative advantages and disadvantages of the two UAS technologies, the results are further generalized in Table 14 which presents a qualitative comparison of the two UAS technologies along a number of dimensions.

Table 14: Summary of the qualitative comparisons between UAS-lidar and UAS-SfM.

	UAS-Lidar	**UAS-SfM**
Cost	high	low
Acquisition time	low	low
User-input processing time	high	moderate
Demand on computing resources	moderate	high
Operational expertise required	high	low
Processing expertise required	high	low
Sensor type	lidar (active)	RGB camera (passive)
Variables of each data point	position & intensity	position & RGB
Georeferencing	position and orientation	position only
Point Density (pts/m^2)	30-250	350-5500
Point Spacing (cm)	6-20	1-5
Can penetrate dense vegetation	yes	no
Reliant on surface texture	no	yes
Reliant on lighting conditions	no	yes

5 Conclusion

This study has identified some of the strengths and weaknesses of UAS-SfM and UAS-lidar for topographical mapping to inform professional surveyors and mappers about the limitations of these newly developed mapping platforms. Although the two techniques typically provide comparable data accuracies (with some differences, as a function of terrain and ground cover type), the application of UAS-SfM is generally less expensive, imposes less stringent requirements for the remote aircraft, requires less expert knowledge and training, and yields higher data densities. Therefore, a primary recommendation from this research is that SfM processing should be the default platform used for typical small scale, less than 2 square kilometers, high density topographic mapping applications based on its low cost, attainable accuracy, and usability. However, UAS-lidar should be used when any of the following conditions apply:

- AOI has homogenous surface texture over a large area
- Data acquisition through thick canopy is required
- Poor light conditions (extreme amounts of shadowing throughout the AOI, data collection at night, etc.) are anticipated

- Surface characteristics derived from intensity returns are required
- Substantial vertical gradients throughout the AOI
- Large amount of tall (relative to flying height) vertical obstructions located throughout the AOI.

Neither of the two options discussed in this research will work for all applications; there are some circumstances that may require the use of both techniques together, possibly in addition to other more well-known mapping techniques, in order to adequately map a desired area. No matter which mapping system is being used, a thorough understanding of the acquisition platform and processing procedures is recommended to produce accurate final products.

As this study focused on empirical analyses, a recommendation for future work is to perform a total propagated uncertainty (TPU) analysis for each discussed mapping platforms. It would also be beneficial to analyze SfM processing limitations through the use of simulations (e.g., Slocum and Parrish, 2017) to determine the specific conditions in which SfM fails and what acquisition parameters could be adjusted to limit these failures (e.g., increased sidelap/overlap, higher GSD, addition of oblique imagery, supplemental ground control, etc.). Through this ongoing work, it is anticipated that both UAS-SfM and UAS-lidar will continue to become increasingly useful technologies to the surveying and mapping community, as their respective strengths, weaknesses and synergies are better understood.

References

Albertz, J. (2007) ‘A Look Back; 140 Years of Photogrammetry’, *PHOTOGRAMMETRIC ENGINEERING & REMOTE SENSING*, 73(5), pp. 504–506.

Alspaugh, D. (2004) ‘A Brief History of Photogrammetry’, in McGlone, C. et al. (eds) *Manual of Photogrammetry*. 5th edn. American Society for Photogrammetry and Remote Sensing, pp. 1–12.

American Society for Photogrammetry and Remote Sensing (2014) *ASPRS Positional Accuracy Standards for Digital Geospatial Data*. 1.0. doi: 10.14358/PERS.81.3.A1-A26.

Everett, T. (2018) *Modified RTKLIB Code - demo5 b29c*. Available at: http://rtkexplorer.com/downloads/rtklib-code (Accessed: 20 June 2018).

Federal Aviation Administration (2016) *Summary of small unmanned aircraft rule*. Available at: https://www.faa.gov/uas/media/Part_107_Summary.pdf.

Federal Geographic Data Committee (FGDC) (1998) *Geospatial Positioning Accuracy Standards, Part 3: National Standard for Spatial Data Accuracy*. Available at: https://www.fgdc.gov/standards/projects/accuracy/part3/chapter3 .

Fonstad, M. A. *et al.* (2012) ‘Topographic structure from motion : a new development in photogrammetric measurement’, *Earth Surface Processes and Landforms*, 38(January), pp. 421–430. doi: 10.1002/esp.3366.

Ghilani, C. D. (2010) *Adjustment Computations: Spatial Data Analysis*. Fifth. John Wiley & Sons.

Harwin, S. and Lucieer, A. (2012) ‘Assessing the accuracy of georeferenced point clouds produced via multi-view stereopsis from Unmanned Aerial Vehicle (UAV) imagery’, *Remote Sensing*, 4(6), pp. 1573–1599. doi: 10.3390/rs4061573.

James, M. R., Robson, S. and Smith, M. W. (2017) ‘3-D uncertainty-based topographic change detection with structure-from-motion photogrammetry: precision maps for ground control and directly georeferenced surveys’, *Earth Surface Processes and Landforms*, 42(12), pp. 1769–1788. doi: 10.1002/esp.4125.

Lowe, D. G. (1999) ‘Object Recognition from Local Scale-Invariant Features’, in *Proceedings of the Seventh IEEE International Conference on Computer Vision*, pp. 1150–1157. doi: 10.1109/ICCV.1999.790410.

Mancini, F. *et al.* (2013) ‘Using Unmanned Aerial Vehicles (UAV) for High-Resolution Reconstruction of Topography: The Structure from Motion Approach on Coastal Environments’, pp. 6880–6898. doi: 10.3390/rs5126880.

Marteau, B. *et al.* (2017) ‘Application of Structure-from-Motion photogrammetry to river restoration’, 515(December 2016), pp. 503–515. doi: 10.1002/esp.4086.

Micheletti, N., Chandler, J. H. and Lane, S. N. (2015) ‘Structure from Motion (SfM) Photogrammetry’, *Geomorphological Techniques*, 2, pp. 1–12. doi: 10.5194/isprsarchives-XL-5-W4-37-2015.

National Geodetic Survey (2018) *OPUS: Online Positioning User Service*. Available at: https://www.ngs.noaa.gov/OPUS/about.jsp.

Pilarska, M. *et al.* (2016) 'The Potential of Light Laser Scanners Developed for Unmanned Aerial Vehicles – The Review and Accuracy', *The International Archives of the Photogrammetry, Remote Sensing and Spatial Information Sciences*, XLII, pp. 87–95. doi: 10.5194/isprs-archives-XLII-2-W2-87-2016.

Renslow, M. S. (ed.) (2012) *Manual of Airborne Topographic Lidar*. American Society for Photogrammetry and Remote Sensing.

Shan, J. and Toth, C. K. (eds) (2008) *Topographic Laser Ranging and Scanning: Principles and Processing*. 1st edn. Taylor & Francis.

Slocum, R. K. and Parrish, C. E. (2017) 'Simulated Imagery Rendering Workflow for Accuracy Assessments UAS-based Photogrammetric 3D Reconstruction Accuracy Assessments', *Remote Sensing*, 9(4), p. 396. doi: 10.3390/rs9040396.

Stewart, J. P. *et al.* (2009) 'Use of Airborne and Terrestrial Lidar to Detect Ground Displacement Hazards to Water Systems', *Journal of Surveying Engineering*, 135(August), pp. 113–124.

Takasu, T. and Yasuda, A. (2009) 'Development of the low-cost RTK-GPS receiver with an open source program package RTKLIB', in *International symposium on GPS/GNSS*. International Convention Center Jeju Korea, pp. 4–6.

Turner, D., Lucieer, A. and Wallace, L. (2014) 'Direct georeferencing of ultrahigh-resolution UAV imagery', *IEEE Transactions on Geoscience and Remote Sensing*, 52(5), pp. 2738–2745. doi: 10.1109/TGRS.2013.2265295.

Westoby, M. J. *et al.* (2012) 'Geomorphology " Structure-from-Motion " photogrammetry : A low-cost , effective tool for geoscience applications', *Geomorphology*. Elsevier B.V., 179, pp. 300–314. doi: 10.1016/j.geomorph.2012.08.021.